EUROPEAN ORGANIZATION FOR NUCLEAR RESEARCH

CERN-EP/80-114
27 June 1980

MEASUREMENTS OF THE TOTAL π-He AND p-He CROSS-SECTIONS AND THE SLOPES OF THE FORWARD DIFFRACTION PEAK AT ENERGIES FROM 50 TO 300 GeV

J.P. Burq[*], M. Chemarin[*], M. Chevallier[*], A.S. Denisov[**], T. Ekelöf[***,†], J. Fay[*], P. Grafström[***,†], L. Gustafsson[†], E. Hagberg[†], B. Ille[*], A.P. Kashchuk[**], G.A. Korolev[**], A.V. Kulikov[**], M. Lambert[*], J.P. Martin[***,*], S. Maury[***,††], J.L. Paumier[††], M. Querrou[††], V.A. Schegelsky[**], I.I. Tkach[**], M. Verbeken[††] and A.A. Vorobyov[**]

ABSTRACT

Differential cross-sections for elastic scattering of pions and protons on helium have been measured at incident momenta ranging from 50 to 300 GeV/c in the t-range $0.008 < |t| < 0.05$ GeV^2. Both recoiled α-particles and forward particles were detected in this experiment. The experimental method provided an absolute normalization of the cross-sections with a precision of 1%. From the analysis of the data, the diffraction slope parameters and total cross-sections have been obtained. The results are compared with Glauber model calculations.

(Submitted to the 20th International Conference on High Energy Physics, Madison, USA, July 1980)

Geneva - 22 June 1980

*) Institut de Physique Nucléaire, IN2P3, Université de Lyon-Villeurbanne, France.
**) Leningrad Nuclear Physics Institute, Gatchina, USSR.
***) At present CERN, Geneva, Switzerland.
†) The Gustaf Werner Institute, University of Uppsala, Sweden.
††) Laboratoire de Physique Corpusculaire, IN2P3, Université de Clermont-Ferrand, Aubière, France.

1. INTRODUCTION

The study of the interaction of high energy hadrons with nuclei is often considered as a possible tool to investigate some features of the hadron-nucleon interaction. In particular, one approach, which is much discussed, is the inelastic shadowing correction[1] to the Glauber theory. It was suggested[2,3] that the s-dependent part of this correction at energies higher than 100 GeV might be related to the triple-Pomeron vertex which plays an important role in the strong interaction theory[4].

From the theoretical point of view it is preferable to study such effects in light nuclei, where the analysis of the results is less complicated. A great deal of the theoretical studies of the shadowing effects concerns the hadron-deuterium scattering. However, the shadowing effects in this reaction are very small, and it is not easy to separate them from other possible corrections to the Glauber model. In hadron-helium scattering the shadowing corrections should be an order of magnitude bigger[5], so there is a hope to study these effects in a more reliable way.

One method to determine the inelastic shadowing correction $\Delta\sigma_{in}$ is to measure the total cross-section σ_{hA} of the hadron-nucleus interaction. Then

$$\Delta\sigma_{in} = \sigma_{hA}^{Gl} - \sigma_{hA}$$

where σ_{hA}^{Gl} is the total cross-section calculated within the Glauber model. Another way is to measure the slope parameter of the diffraction cone, since the inelastic shadowing should increase the slope parameter. To our knowledge, there was so far no absolute measurements of the total cross-section for hadron-helium interactions at high energies.

The elastic p-^4He differential cross-sections have recently been measured in a jet-target experiment[6] at Fermilab in the energy range from 40 to 400 GeV. The p-^4He cross-sections were normalized to the p-p cross-sections using a $(^4He + {}^1H)$ gas mixture in the jet. The measured differential cross-sections were found to be considerably ($\sim$15%) below the cross-sections calculated within the Glauber model, which indicated an important role of the inelastic shadowing correction to the p-^4He total cross-section. This correction proved to be practically independent on s. In fact, this required either to assume some rapid increase of the inelastic correction below 40 GeV, or to consider the observed

effect not to be due to inelastic shadowing, but a result of some defects in the Glauber model which do not depend on energy.

Another problem revealed by the jet-target experiments is the relative shrinkage of the diffraction cones in p-p, p-d, and p-^{4}He scattering. If one parametrizes the s-dependence of the slope parameter as $b = b_0 + b_1 \ln s$, then according to Reference (6)

$$b_1 \text{ (p-p)} = 0.56 \pm 0.05 \text{ GeV}^{-2}$$

$$b_1 \text{ (p-d)} = 0.96 \pm 0.02 \text{ GeV}^{-2}$$

$$b_1 \text{ (p-}^4\text{He)} = 1.13 \pm 0.18 \text{ GeV}^{-2}$$

In the framework of inelastic shadowing it is difficult to explain why there is a big difference between b_1 (p-d) and b_1 (p-p), but no difference between the b_1 (p-d) and b_1 (p-^{4}He) parameters.

A study of π-p, π-^{4}He, p-p, and p-^{4}He small-angle scattering has recently been undertaken in the WA9 and NA8 experiments at the CERN Super Proton Synchrotron (SPS). The main purpose of these experiments was to measure the real part in the $\pi^- p$ forward amplitude, but also the π-p, π-^{4}He, p-p, and p-^{4}He slope parameters could be determined from the experimental data. Here, we report on the results of the analysis of the π-^{4}He and p-^{4}He scattering data. The elastic scattering differential cross-sections have been measured in the t-range $0.008 < t < 0.05$ GeV^2 at energies ranging from 50 to 300 GeV (π-^{4}He) and from 100 to 300 GeV (p-^{4}He). The cross-sections were normalized absolutely with a precision of 1% (NA8) to 2% (WA9), which made it possible to determine, through the optical theorem, the total cross-section of the π-^{4}He and p-^{4}He interactions. Also, the slope parameter of the diffraction cone has been determined. Due to the absolute normalization of the cross-sections, the data allowed quantitative comparison with the results of calculations with the Glauber model. Using this model, we determined the slope parameters for pion-nucleon and proton-nucleon scattering from the π-^{4}He and p-^{4}He data and compared the obtained results with recent direct measurements of the π-p and p-p slope parameters.

2. THE EXPERIMENTAL SET-UP

Both the low-energy recoil α-particle and the high-energy beam particle are detected and measured in this experiment. In Figure 1 is given a schematic lay-

out of the NA8 experiment, showing the recoil detector IKAR, the forward MWPC-magnet spectrometer, the trigger scintillators, and the particle identifiers. The lay-out of the WA9 experiment differed only in some details, and has already been described elsewhere[7], where the first results on the $\pi^- p$ scattering were reported.

The recoil detector[7,8] is an ionization chamber which serves as a gas target and as a detector at the same time. The chamber was filled with a mixture of He (8 atm) and H_2 (2 atm). Neither of the gases had an impurity content exceeding 10^{-6}. Two of the six separate ionization chamber cells in IKAR are shown in Figure 2. Each cell contains an anode plate and a cathode plate, 12 cm apart, mounted perpendicularly to the beam direction. An earthed wire grid is placed 2 cm away from the anode. When an incident beam particle makes an elastic collision with a target ^{4}He nucleus, this nucleus recoils out in a direction almost parallel to the electrode plates, ionizing the gas along its path. The electron track thus created in the gas will start to drift in the high electric field towards the anode plate. The unshielded cathode will feel a signal immediately after the collision as the electrons start to separate from the ions, whereas the anode signal will appear only when the electrons drift through the grid. The electron drift time from cathode to anode is 22 μsec. The anode plate is divided into three rings (A, B, and C) that are mounted concentrically around the beam axis.

The recoil kinetic energy T_R can be derived from the pulse height of the anode A signals. The ^{4}He recoils were detected in the energy interval $1\ \text{MeV} \lesssim T_R \lesssim 6\ \text{MeV}$. The range of the ^{4}He recoil did not reach outside the anode A zone, and anodes B and C were used only to reject long-range background particles. The recoil track projection X_R on the beam axis can be obtained from the rise-time of the anode A pulse, as this time is a measure of the inclination of the electron track as it traverses the grid. Furthermore, the delay of the anode pulse with respect to the passage of the beam particle is a measure of the distance Z_R of the recoil track from the cathode.

Alpha sources (^{234}U) that had been deposited on each cathode were used for the T_R-scale calibration. In two cells, α-sources had been deposited also on the grids to control the amount of electrons lost during their drift in the cathode-grid space. Such losses are the result of adhesion of the electrons to electro-negative impurities such as O_2 contained in the gas mixture. In the present case, the losses due to electron adhesion were about 0.9% per 10 cm drift.

The beam enters and leaves the pressure vessel through steel windows that are 270 μm thick and 80 mm in diameter. In the region where the beam traverses the chamber electrodes, these windows are made of thin aluminium foils of a total thickness of 360 μm. The ionization energy left in the gas by a relativistic particle is about 50 keV in each ionization chamber cell. The corresponding signals on the chamber electrodes are suppressed by sending pulses of the same magnitude, but of opposite polarity, to the electrodes each time a beam particle passes through the chamber. The fluctuations of the ionization produced by the beam particles determined the energy resolution of IKAR at high beam intensities. At a beam intensity of 10^6 particles per 1 s spill, the resolution was 130 keV (FWHM), independently on the pulse height. The corresponding resolution in the four-momentum transfer squared was Δt (FWHM) $\approx 10^{-3}$ GeV^2.

The resolution in the X_R measurements was $\sigma_{X_R} = (1.5 \div 3)$ mm, and that in the Z_R determination was $\sigma_{Z_R} = 0.3$ mm. The effective target length in each cell was defined as $Z_{min} \leq Z_R \leq Z_{max}$, where $Z_{min} = 10$ mm and $Z_{max} = 90$ mm. The electron drift velocity W was determined from the experimental data with a precision of 0.2%, the cathode-grid distance d was known with a precision of 0.1% ($d = 100.0 \pm 0.1$ mm), and the gas pressure was measured with a precision of 0.1%, which made it possible to determine the number of He-nuclei in the effective target length with a precision of 0.4%.

The forward spectrometer served to determine the scattering angle θ and the momentum p_{out} of the forward scattered particles. Six blocks of multiwire proportional chambers (MWPCs) (PC1-PC6) were used to measure the horizontal (x_1-x_6) and vertical (y_1-y_5) co-ordinates of the forward particle. The values of θ and p_{out} were obtained using the following relations:

$$\theta^2 = \theta_x^2 + \theta_y^2 - 2\sigma_{\theta_{proj}}^2 \tag{1}$$

$$\theta_x = \frac{x_4 - x_3}{L_2} - \frac{x_2 - x_1}{L_1}, \qquad \theta_y = \frac{y_4 - y_3}{L_2} - \frac{y_2 - y_1}{L_1} \tag{2}$$

$$p_{out}^{-1} = \text{const} \left[\frac{x_6 - x_5}{L_3} - \frac{x_4 - x_3}{L_2} \right] \tag{3}$$

Here, $\sigma_{\theta_{proj}}$ is the angular resolution of the forward spectrometer; L_1, L_2, L_3 are the distances between the PC1-PC2, PC3-PC4, and PC5-PC6 blocks, respectively.

Blocks PC1, PC2, and PC3 contained four MWPCs each (two chambers in the X-plane and two chambers in the Y-plane). Block PC4 contained six such chambers. The wire spacing in all MWPCs was 1 mm. All these chambers were tilted around the central wire by an angle $\psi \approx 10^{\circ}$ with respect to the beam direction. This increased the probability for a two-wire hit to 50%, which had the effect of improving the spatial resolution of the chambers[9]. Furthermore, adjacent chambers with parallel wires were shifted by 0.25 mm with respect to each other. The resulting spatial resolution of each MWPC block was FWHM $\simeq$ 0.25 mm. Block PC5 contained six X chambers and two Y chambers, while block PC6 contained only two X chambers. The useful areas of the chambers were 32×32 mm^2 in PC1 and PC2, 48×48 mm^2 in PC3, 160×160 mm^2 in PC4, 192×192 mm^2 in PC5, and 287×287 mm^2 in PC6. The alignment of all the MWPCs was performed using beam particles, and the resulting precision was better than 50 μm. The angular acceptance of the forward spectrometer was close to 100% for the t-range under investigation. In order to minimize hadronic interactions of the beam particles with the air and to reduce the multiple Coulomb scattering, vacuum tubes were used between the MWPC blocks. For the same purpose, a He bag was used inside the magnets Bend 5-Bend 8. The momentum resolution of the forward spectrometer was $\sigma_{p_{out}}/p_{out} = 0.2\text{-}0.3\%$. The resolution in the forward scattering angle measurements varied from $\sigma_{\theta_{proj}} = 32$ μrad at $p = 100$ GeV/c to $\sigma_{\theta_{proj}} = 18$ μrad at $p = 300$ GeV/c.

The high-resolution beam spectrometer, provided in the incident beam as a general facility, gave information on the momentum of each beam particle within the momentum bite defined by the momentum slit. In the experiment, the momentum defining collimator was varied in order to maintain the intensity in the secondary beam line at a constant level, and as a result the momentum bite varied between $\Delta p = \pm 0.2\%$ and $\Delta p = \pm 1\%$. The resolution of the beam spectrometer was estimated from the data to be $\sigma_p/p \simeq 0.05\%$. The mean absolute momentum of the beam particles was determined from the data of the present experiment with a precision of 0.15%. The details of this procedure can be found in a special report[10]. Table I shows the results of these measurements. Here, p^* and p_o are the measured and the nominal value of the beam particles momentum, respectively.

For identification of the incident hadrons, two differential Čerenkov counters (CEDAR I and CEDAR II) and two threshold counters (TH1 and TH2) were used. Muons were identified with two scintillator counters of dimensions 420×410 mm^2 and 480×510 mm^2 interspaced by a 1 m thick iron block. These counters were placed

downstream of the beam stopper. The total thickness of iron in the beam stopper was about 5 m. For identification of electrons, an electromagnetic shower detector was used, consisting of 13 scintillator counters 600×600 mm^2 in dimension, interspaced by lead plates with a thickness of 15 to 50 mm, followed by 5 scintillator counters of 700×700 mm^2, interspaced by 50 to 100 mm thick iron blocks.

The beam particles interacting with material in the beam line upstream of IKAR may produce showers, which reach IKAR, thus creating ionization pulses which constituted the most important background in the experiment. To protect the chamber against the beam halo particles, a 3.2 m long iron collimator with a 40 mm channel for the beam was installed just upstream of the ionization chamber. Further elimination of the shower background was achieved with a shower detector A3 placed just downstream of IKAR. This detector was made of four separate square scintillators, mounted as the four quadrants in a square of dimensions 650×650 mm^2 with a central opening of 50×50 mm^2. A lead plate of 20 mm thickness was placed in front of each of the four A3 counters. These counters were used to form a coincidence signal, when at least three hits were registered. If such a coincidence appeared during the registration time of IKAR (25 μsec), the event was rejected.

A set of scintillator counters S1A, S1B, S2A, S2B, A1, A2, A3 was used to trigger the system and to define the incident beam traversing IKAR inside the beam channel. The scintillators S1A and S1B were 1.5 mm thick and had a surface of 32×32 mm^2. The dimensions of S2A and S2B were 330×330 mm^2; those of A1 were 220 mm outer diameter with a 30 mm diameter hole; for A2 they were 220 mm outer diameter with a 40 mm hole. No veto counter was used downstream of IKAR, except A3, with the aim to avoid killing of events accompanied by bremsstrahlung gammas. For this reason, the A3 counter was used only on a coincidence majority level 3. It was checked in a special run, that on this majority level the A3 counter did not affect the detection efficieny for good events. Special care was also taken to provide 100% efficiency of the counter S2 ≡ S2A ∪ S2B. The global and the local efficiencies of this counter were under permanent control.

3. MEASUREMENTS AND RESULTS

The secondary beam used in the experiment was derived from a 400 GeV primary proton beam. The beam was focused onto IKAR, and the dimensions of the beam spot

at focus were about 10×10 mm^2. The intensity of the beam was 8×10^5 particles over an effective spill length of 800 ms, and the burst cycle time was 10.8 s.

The trigger was formed on three sequential levels. The first-level trigger was $S1A \cdot S1B \cdot (S2A \cup S2B) \cdot \overline{A1} \cdot \overline{A2} \cdot \overline{A3}$. This trigger strobed PC1-PC4 and gave a start signal to a Special Digital Processor Unit (SDPU)[11]. The SDPU received information from PC1, PC2, and PC4, and calculated within 250 ns whether or not the scattering angle was bigger than a preset threshold value. If this was the case, a second-level trigger was produced. With a threshold value corresponding to $|t| = 3 \times 10^{-3}$ GeV^2, the reduction in the trigger rate due to the SDPU was around a factor of 250. The probability for a good event to be rejected by the SDPU was estimated with a Monte-Carlo simulation taking into account the experimental angular resolution of the forward spectrometer. The number of rejected events in the measured t-range was found to be negligible.

The second-level trigger strobed the MWPCs in blocks PC5, PC6, BS1-BS4, and opened the gates of the IKAR shapers. If a cathode signal arrived within 4 μs, followed by an anode signal within 25 μs, the data acquisition system was triggered. The reduction in the trigger rate due to the IKAR trigger requirement was about a factor of 25, and as a result about 100 events were sent on tape every burst. These events contained about 30 elastic scatterings having a recoil energy of $1 \text{ MeV} \lesssim T_R \lesssim 6 \text{ MeV}$ and longitudinal track positions of $1 \text{ cm} \lesssim Z_R \lesssim 9 \text{ cm}$.

In the data analysis, the events were first selected using the following criteria:

i) the forward particle track should be reconstructable in each PC block;
ii) the forward particle should be neither a muon nor an electron;
iii) the momentum of the scattered particle should be within ±5% of the momentum of the incident beam;
iv) there should be no pulses on the electrodes B and C of IKAR with amplitudes higher than .5 MeV;
v) the longitudinal recoil track position should be within $1 \text{ cm} \lesssim Z_R \lesssim 9 \text{ cm}$.

Most of the events selected with such requirements are elastic scatterings, as can be seen from Figures 3 and 4, where correlation matrices of T_R versus X_R and of T_R versus the difference $\Delta = |(p_0\theta)^2/2M_R - T_R|$ are presented for $\pi^- - {}^4$He scattering at $p_0 = 250$ GeV/c. The final selection was performed cutting the tails in these two-dimenstional distributions. This was done using the

χ^2-distribution method. The χ^2-distribution was formed by the two terms represented in Figures 3 and 4. This distribution is shown in Figure 5. The cut in the χ^2-distribution was put at $\chi^2 = 15$. The final result was proved to be independent on the cut position chosen within reasonable limits.

The next step in the analysis was subtraction of the background at $\chi^2 < 15$ and correction for the inefficiency of the apparatus. This was done by "test events" which played an important role in the experiment. In parallel with the data acquisition, test pulses were generated by a test generator and sent to the IKAR electrodes. These pulses simulated recoils of different energies and positions in each of the 6 cells of IKAR. Each recoil test signal was sent in coincidence with a real incident beam particle. Of the order of 10 such triggers were generated during each accelerator pulse, and the data from all detectors of the experiment were read out on the tape as for the real trigger events. The test events gave a possibility to measure the inefficiency of each part of the equipment, and to control different kinds of rejections, such as rejection of the events with incident trajectories not satisfying the requirement of 100% angular acceptance ($\sim$1% correction) or rejection of the events with $\chi^2 > 15$ ($\sim$1.5% correction). The total correction for the inefficiency was about 15% and it was measured with an accuracy better than 0.5%. To determine the contribution of the background under the χ^2-peak, we subtracted the χ^2-distribution of the test events from those of the physical events, and the remaining background was fitted with a constant level in the region $15 < \chi^2 < 50$. This level was then accepted as the level of the background also at $\chi^2 < 15$ (see Figure 5). The correction due to the background was typically 1% for $T_R \simeq 1$ MeV and 0.5% for $T_R \simeq 6$ MeV.

We estimated possible contributions to the selected events due to semi-coherent reactions of the type $h + {}^4He \to h + {}^4He^* \to h + p + {}^3H$ or $h + {}^4He \to h + n + {}^3He$. This contribution was shown to be less than o.1% for the first reaction and less than 0.5% for the second one.

To determine the differential cross-sections $d\sigma/dt$, we used the recoil energy as a measure of the four-momentum transfer:

$$|t| = 2 M_R T_R \qquad (4)$$

where M_R is the recoil mass. The T_R-scale was calibrated in the following way[10]. For the events with the recoil energy T_R equal to the energy E_α of the α-particles emitted from the α-source, the α-source signals represent an

absolute calibration reference which does not rely on any assumptions about the relation between ionization charge and recoil energy, or about the linearity of the pulse-height registration electronics. This reference for T_R at $T_R^* = E_\alpha$ will in turn provide an absolute reference for a certain value t^* of the four-momentum transfer squared:

$$|t^*| = 2\, M_\alpha\, E_\alpha \,. \tag{5}$$

At any fixed value of the beam momentum there will be a certain angle θ^* corresponding to t^*. In practice, the value of θ^* was determined from the correlation between θ and T_R in the measured data as the mean scattering angle corresponding to T_R^*. Knowing this angle, we have the scaling law which provides an absolute determination of the whole T_R-scale under the assumption that the θ-scale is strictly linear:

$$T_R = E_\alpha\, (\theta/\theta^*)^2 \tag{6}$$

Such calibration showed that the ionization produced by the He recoils in the He-H mixture is a linear function of their energy:

$$T_R = (V_R - V_0)\, \frac{E_\alpha}{V_\alpha - V_0}\, \left[\, 1 - \delta(Z_R)\right] \,, \tag{7}$$

where

E_α = $(E_\alpha^{(0)} - \Delta_{abs})$ is the α-particle energy corrected for the energy absorption in the matter of the α-source, $E^{(0)} = 4.777$ MeV (^{234}U-source);

V_α = the mean amplitude of pulses produced by the α-particles from the cathode source;

V_R = the amplitude of the pulse produced by a ^{4}He recoil;

V_0 = $V_\alpha \cdot E_0/E_\alpha$, $E_0 = 40$ keV;

$\delta(Z_R)$ = a correction which takes into account both the loss of electrons through adhesion and the limited transparency of the grid. As the adhesion of the electrons could be measured and controlled, $\delta(Z_R)$ is a known function of Z_R. In the present case, the correction was $\delta(Z_R) \simeq 0.1\% \cdot Z_R$ (cm).

The absorption in the α-sources was determined experimentally by analysing the angular dependence of the α-pulse amplitude. The absorption correction averaged over all the chamber cells was found to be Δ_{abs} = 10 keV ± 5 keV. The errors in the absolute calibration of the t-scale by this method were estimated to be ∿0.1% at $|t|$ = 0.04 GeV^2 and 0.5% at $|t|$ = 0.01 GeV^2 which corresponds to the errors of ±0.1 GeV^{-2} in the slope parameter and ±0.25% in the total cross-section determination.

The differential cross-sections measured in this experiment are presented in Table II and in Figures 7 and 8. The errors shown in Table II are statistical only. The π-He cross-sections have been corrected for the bremsstrahlung effect. Figure 6 shows the $p\text{-}p_{out}$ distribution for the events left after the χ^2-cut. As can be seen in the figure, the tail of the distribution is very small. The magnitude and the t-dependence of the tail agree with the assumption that most of the tail is due to bremsstrahlung of the scattered pions. Furthermore, a comparison between the π-^{4}He data and the p-^{4}He data strengthens this assumption. The correction takes into account the bremsstrahlung events that are rejected by the momentum cut. The formulae employed were derived from a general expression given in Reference (12)

$$(d\sigma/dt)^{corr} = (d\sigma/dt)^{meas} \left[1 + \delta(t) \right] \tag{8}$$

where $(d\sigma/dt)^{corr}$ and $(d\sigma/dt)^{meas}$ are the corrected and the measured cross-sections, respectively, and

$$\delta(t) = \frac{2\alpha}{\pi} \cdot \ln (p/\Delta p) \left\{ \frac{(2m_\pi^2 - t)}{Q} \ln \frac{Q - t}{Q + t} - 1 \right\} \tag{9}$$

where

$Q = (t^2 - 4t \cdot m_\pi^2)^{\frac{1}{2}}$;

α = the fine structure constant;

m_π = the pion mass;

Δp = the maximum momentum loss accepted by the momentum cut.

In our case $\Delta p/p = 0.05$, and the bremsstrahlung correction $\delta = 0.2\%$ at $|t| = 0.008$ GeV^2 and $\delta = 0.8\%$ at $|t| = 0.048$ GeV^2.

4. DISCUSSION

The measured differential cross-sections were fitted with the Bethe interference formula

$$d\sigma/dt = N \cdot |f_c e^{i\phi} + f_n|^2 \tag{10}$$

where f_n is the nuclear scattering amplitude and f_c is the Coulomb scattering amplitude:

$$f_c = \frac{2Z_1 \cdot Z_2 \cdot \alpha \cdot \hbar \cdot \sqrt{\pi}}{t} G_h(t) \cdot G_{He}(t) \tag{11}$$

Here α is the fine structure constant, Z_1 and Z_2 are the charges of the projectile and of the target nucleus, respectively, $(Z_1 \cdot Z_2 = \pm 2)$, $G_h(t)$ is the electromagnetic form factor of the projectile[13]:

$$G_p(t) = (1 + |t|/0.71)^{-2} ,$$

$$G_\pi(t) = (1 + |t|/0.59)^{-1} ,$$

$G_{He}(t)$ is the ^4He form factor:

$$G_{He}(t) = \exp(r_{He}^2 \cdot t/6)$$

where $r_{He} = 1.644$ fm[14] is the r.m.s. charge radius of the ^4He-nucleons, ϕ is the Bethe phase[15]:

$$\phi = -Z_1 Z_2 \cdot \alpha \left[\ln(B|t|) + 0.577 \right], \tag{12}$$

$$B = (R_s^2 + r_\pi^2 + r_{He}^2)/6$$

where R_s is the effective strong interaction r.m.s. radius and r_π is the pion r.m.s. charge radius. In fact, the value of B is close to the value of the hadron-helium slope parameter, and in the present calculations we put $B = 33$ GeV^{-2}.

The normalization parameter N was constrained to be unity ±1% for the data from the NA8 experiment, and ±2% for the data from the WA9 experiment. The nuclear scattering amplitude was taken in two different forms. In the phenomenological fit it was

$$f_n = \frac{\sigma_{tot}}{4\hbar\sqrt{\pi}} (i + \rho) \exp\left(\frac{bt}{2}\right) \qquad (13)$$

where σ_{tot} is the total hadron-helium cross-section, b is the logarithmic slope of the hadron-helium diffraction cone, and ρ is the ratio of the real to imaginary part of the hadron-helium forward scattering amplitude.

The parameter ρ was chosen as follows. For the π-^{4}He scattering we used

$$\rho = \frac{\rho_{\pi^- p} + \rho_{\pi^+ p}}{2}$$

where $\rho_{\pi^\pm p}$ was taken from the dispersion relation calculations by Höhler et al.[16]. For the p-^{4}He scattering we have taken the data on ρ_{pd} from reference (17) assuming $\rho = \rho_{pd}$.

The parameters σ_{tot} and b were free in the fits. The results of the fits are presented in Table III. It was checked that the results are not sensitive to the removal from the fit of the first 5 points or the 5 last points in $d\sigma/dt$.

Of course, the values of σ_{tot} obtained from the exponential fit should be considered only as a first approximation. The extrapolation to the optical point would be more precise if one replaces in equation (13) $\exp \frac{bt}{2}$ by $\exp \frac{b_0 t + ct^2}{2}$, where c is the curvature parameter. It was not possible to determine c from our data as the t-range is too small for such purposes. For p-^{4}He scattering, this parameter was determined in the jet-target experiment[6]. For example, $c = (-24\pm3)$ GeV^{-4} at an energy of 300 GeV. With this value for c, we have obtained for p-^{4}He scattering at 300 GeV: $b_0 = (33.8\pm.2)$ GeV^{-2}; $\sigma_{tot} = (131.1\pm.8)$ mb; $\chi^2/N = 62/53$. Comparison with the results from Table III shows that the fit with the curvature parameter is slightly better than the exponential fit and that the new fit reduces σ_{tot} by 0.9 mb.

As we shall see now, the results on σ_{tot} from the fit with the curvature parameter are not different from those obtained with the Glauber fit. In this fit the nuclear scattering amplitude f_n in equation (10) was represented by the Glauber formula:

$$f(t) = i \cdot \frac{\sqrt{\pi\hbar}}{2} \cdot (R^2 + 2b_{hN}) \exp\left(-\frac{R^2 t}{16}\right) \cdot \qquad (14)$$

$$\cdot \left\{ \sum_{m=1}^{4} K_m \begin{bmatrix} 4 \\ m \end{bmatrix} \frac{(-1)^{m+1}}{m} (1 - i\rho_{hN})^m \left(\frac{\sigma_{hN}}{2\hbar^2\pi(R^2 + 2b_{hN})}\right)^m \cdot \exp\left(\frac{(R^2 + 2b_{hN})}{4m} t\right) \right\}$$

Here $R^2 = \left[\frac{8}{9} (r_{He}^2 - r_p^2) \right] / \hbar^2$

($r_{He} = 1.644$ fm, $r_p = 0.8$ fm, $R = 6.87$ GeV^{-1}) .

The elementary hadron-nucleon amplitude was written in the form:

$$f_{hp} = f_{hn} = f_{hN} = \frac{\sigma_{hN}}{4\hbar\sqrt{\pi}} (i + \rho_{hN}) \exp (b_{hN} \cdot t/2) \qquad (15)$$

where $\sigma_{hN} = \frac{\sigma_{hp} + \sigma_{hn}}{2}$, the total cross-sections σ_{hp} and σ_{hn} taken from reference (18). The parameter ρ_{hN} is identical to ρ which was described before.

The parameters K_m are introduced to take into account the contribution due to the inelastic intermediate states. We put $K_1 = K_3 = K_4 = 1$ and let K_2 be free. The elementary slope parameter b_{hN} was the second free parameter in the fits. The results of the fits are shown in Table IV. The total cross-sections were calculated using the optical theorem:

$$\sigma_{tot} = 4 \hbar \sqrt{\pi} \, \mathrm{Im} f_n (0)$$

and the results are indicated in Table IV. The comparison of the Glauber fit and the phenomenological fit with the curvature parameter (p-^{4}He, 300 GeV) shows that both fits give the same values of σ_{tot} and χ^2/N. Using this as an argument in favour of the Glauber fit, we consider σ_{tot} obtained from the Glauber fit as our final results.

In Table IV are also given the total cross-sections σ_{tot}^{Gl} calculated with the Glauber model. In these calculations, the slope parameters b_{hN} were taken from reference (19) (see also Figures 11 and 12) and all the coefficients $K_m = 1$.

Using the values of σ_{tot} and σ_{tot}^{Gl} given in Table IV, we can calculate $\Delta\sigma_{in} = \sigma_{tot}^{Gl} - \sigma_{tot}$ which is usually considered as the inelastic shadowing correction. The results are plotted in Figure 9. The data of Jenkins et al.[6] for p-^{4}He scattering are also shown there. As can be seen from the figure, the results of these two experiments are quite different. The difference in the measured values of $\Delta\sigma_{in}$ corresponds to $\sim$10% difference in the absolute normalization of the differential cross-sections. We remind that in the jet-target experiment the normalization was only relative, and it is not excluded that the geometrical dimensions of the helium and hydrogen jets could be different. Anyhow,

our data show that the inelastic shadowing correction is only about 3 mb in $p-^4He$ scattering and about 2.5 mb in $\pi^- - ^4He$ scattering.

Both our experiment and the jet-target experiment indicate no strong s-dependence of the inelastic shadowing correction. If we represent the s-dependence of $\Delta\sigma_{in}$ by

$$\Delta\sigma_{in} = \Delta\sigma_0 + \Delta\sigma_1 \ln s$$

then we obtain from the fit to our experimental points:

$$\Delta\sigma_1(p\text{-}He) = (0.2\pm1) \text{ mb} ,$$

$$\Delta\sigma_1(\pi\text{-}He) = (1\pm0.4) \text{ mb} .$$

Similar fit to the data of Jenkins et al.[6] gives:

$$\Delta\sigma_1(p\text{-}He) = (0.6\pm0.4) \text{ mb} .$$

Figure 10 displays the exponential slope parameters determined from the phenomenological fits. Also plotted are the $p-^4He$ data from the jet-target experiment corresponding to $|t| = 0.035$ GeV^2. There is a reasonable agreement between the two experiments in the slope measurements. The $p-^4He$ data exhibit the shrinkage effect:

$b_1(p\text{-}He) = (0.7 \pm0.3)$ GeV^{-2} from our data, and

$b_1(p\text{-}He) = (1.13\pm0.18)$ GeV^{-2} from the FNAL data.

On the other hand, the shrinkage effect in $\pi^- - ^4He$ scattering was found to be smaller:

$$b_1(\pi\text{-}He) = (0.3 \pm0.2) \text{ GeV}^{-2} .$$

In the Glauber theory the shrinkage of the hadron-helium diffraction cone reflects the shrinkage of the elementary hadron-nucleon cone. However, some additional shrinkage may appear due to the s-dependent part of the inelastic shadowing correction. For small t-values this additional shrinkage can be represented by

$$\Delta b_1(\mathrm{hHe})\Big|_{t\approx 0} \approx b_{\mathrm{hHe}} \cdot \frac{\Delta\sigma_1(\mathrm{hHe})}{4\sigma_{\mathrm{hN}}} \qquad (16)$$

As we already pointed out $\Delta\sigma_1(\mathrm{hHe})$ was found to be small. With $\Delta\sigma_1(\mathrm{p\text{-}He}) = 0.6$ mb one obtains from equation (16):

$$\Delta b_1(\mathrm{p\text{-}He})\Big|_{t\approx 0} \approx 0.13\ \mathrm{GeV}^{-2}\ ,$$

which cannot explain the difference between $b_1(\mathrm{p\text{-}p}) = 0.56\ \mathrm{GeV}^{-2}$ and $b_1(\mathrm{p\text{-}He}) = 1.13\ \mathrm{GeV}^{-2}$ observed in the jet-target experiments. There is a similar situation in p-d scattering. According to reference (5), the values of $\Delta\sigma_{in}(\mathrm{hd})$ and $\Delta\sigma_1(\mathrm{hd})$ should be an order of magnitude smaller as compared to the hadron-helium case. Using our helium data, we then obtain:

$$\Delta\sigma_{in}(\mathrm{p\text{-}d}) \approx \Delta\sigma_{in}(\pi\text{-}\mathrm{d}) \approx 0.3\ \mathrm{mb}$$

$$\Delta\sigma_1(\mathrm{p\text{-}d}) \approx \Delta\sigma_1(\pi\text{-}\mathrm{d}) \approx 0.1\ \mathrm{mb}\ .$$

The additional shrinkage due to the inelastic shadowing in deuterium is given by

$$\Delta b_1(\mathrm{hd})\Big|_{t\approx 0} \approx b_{\mathrm{hd}} \cdot \frac{\Delta\sigma_1(\mathrm{hd})}{2\sigma_{\mathrm{hN}}} \qquad (17)$$

Using this equation we obtain:

$$\Delta b_1(\mathrm{p\text{-}d})\Big|_{t\approx 0} \approx 0.05\ \mathrm{GeV}^{-2}$$

which is negligible if compared with the difference between $b_1(\mathrm{p\text{-}p}) = 0.56\ \mathrm{GeV}^{-2}$ and $b_1(\mathrm{p\text{-}d}) = 0.96\ \mathrm{GeV}^{-2}$ reported in reference (6).

To explain the above described situation one can of course assume, that the Glauber theory, in the present form, is not able to reproduce the elastic-scattering mechanism at high energies. In fact, this was the conclusion made by the authors of reference (6). However, there may be another explanation which, in our opinion, cannot be disregarded: the problem can be solved if one assumes that in the momentum range $40 < p_{\mathrm{lab}} < 200$ GeV/c the proton-proton shrinkage parameter was underestimated in the previous experiments, and that the real value of $b_1(\mathrm{p\text{-}p})$ is close to $b_1(\mathrm{p\text{-}d})$. This assumption can only be verified by new

measurements of the proton-proton slopes. The recent data of Fajardo et al.[19] seem to support such an explanation. The p-p slope parameters obtained in this experiment in the momentum range $100 < p < 200$ GeV/c proved to be higher than those measured in the jet-target experiments. In combination with the data available at lower energies, this gives much bigger p-p shrinkage parameters. The p-p slope parameters at 100, 150, 250, and 300 GeV/c have also been measured in the NA8 experiment, but the analysis of the data is not jet finished.

Assuming that the Glauber theory with the inelastic shadowing correction is an adequate way to describe the small-angle elastic scattering, we have determined the proton-nucleon and the pion-nucleon slopes from our $p-^4He$ and $\pi-^4He$ data. The results are shown in Figures 11 and 12. The comparison with the p-p and $\pi^{\pm}p$ slopes obtained by Fajardo et al.[19], and also with the π^-p slope from the NA8 experiment is encouraging. Figures 11 and 12 also display the parameter K_2 obtained from the Glauber fit to our experimental data. One can see, that in the case of the $p-^4He$ scattering it is enough to increase the double scattering term in the Glauber formula by $\sim$10% to describe well the experimental data. In the case of the $\pi-^4He$ scattering, the relative importance of the inelastic scattering correction is somewhat bigger ($K_2 \approx 1.25$).

In conclusion, we find that the Glauber theory with the inelastic shadowing correction describes well the hadron-helium small angle elastic scattering. The inelastic shadowing correction is relatively small and has no strong s-dependence. The hadron-nucleon slope parameters obtained from the Glauber analysis of the helium data are in good agreement with recent direct measurements of the hadron-proton slope parameters.

REFERENCES

1) E.S. Abers et al., Nuovo Cimento 42A (1966) 363.
V.N. Gribov, Sov.Phys. JETP 29 (1969) 483; Zh.Eksp.Teor.Fiz. 56 (1969) 892.

2) J. Kwiecinski et al., Nucl.Phys. B78 (1974) 251.

3) Ya.I. Azimov et al., JETP Letters 23 (1976) 114; Pis'ma Zh.Eksp.Teor.Fiz. 23 (1976) 131.

4) V.N. Gribov, Proc. 16th Int. Conf. on High Energy Physics, Batavia, USA, 1972, Vol. 3, 491.

5) E.M. Levin and M.I. Strikman, Leningrad Nuclear Physics Institute, Report 203 (1975).

6) V.A. Nikitin, Proc. Int. Conf. on High Energy Physics, Geneva, 1979, p. 547.
E. Jenkins et al., to be published in Phys.Rev.

7) J.P. Burq et al., Phys. Lett. 77B (1978) 438.

8) A.A. Vorobyov et al., Nucl. Instr. Methods 119 (1974) 509.

9) E.A. Damaskinsky et al., Nucl. Instr. Methods 130 (1975) 611.

10) J.P. Burq et al., Preprint CERN-EP/80-83, submitted to Nucl. Instr. Methods.

11) A.P. Kashchuk and V.L. Golovtsov, Leningrad Nuclear Physics Institute, Report 395 (1978).

12) M. Sogard, Phys.Rev. D9 (1974) 1486.

13) M.M. Nagels et al., Nucl. Phys. B109 (1976) 1.

14) A. Bertin et al., Phys. Lett. 55B (1975) 411.

15) M. Locher, Nucl. Phys. B2 (1967) 525.

16) G. Höhler et al., Karlsruhe Kernforschungszentrum, Report KFK 2457 (1977).

17) D. Gross, Phys.Rev.Lett. 41 (1978) 217.

18) A.S. Carroll et al., Phys. Lett. 61B (1976) 303 and 80B (1979) 423.

19) L.A. Fajardo et al., Fermilab-Pub-80/27-EXP, 7120, submitted to Phys.Rev.

Table I

Polarity	p_0 (GeV/c)	$\frac{p^* - p_0}{p_0}$ (%)	p^* (GeV/c)
-	100	+0.30 ± 0.05	100.30 ± 0.05
+	100	+0.20 ± 0.05	100.20 ± 0.05
-	150	+0.35 ± 0.12	150.52 ± 0.18
+	150	+0.35 ± 0.05	150.52 ± 0.08
-	200	+0.35 ± 0.06	200.79 ± 0.12
-	250	+0.15 ± 0.05	250.38 ± 0.13
+	250	+0.15 ± 0.07	250.38 ± 0.18
-	280	+0.23 ± 0.10	280.64 ± 0.28
-	300	-0.04 ± 0.06	299.88 ± 0.18
+	300	-0.08 ± 0.06	299.76 ± 0.18

TABLE II

T GEV**2	CROSS SECTION MB/(GEV**2)	CROSS SECTION MB/(GEV**2)
.0078		678.0 ± 11.6
.0086		658.8 ± 11.3
.0093		660.5 ± 11.3
.0101		641.2 ± 11.1
.0108	620.0 ± 11.5	609.5 ± 10.8
.0116	601.5 ± 11.3	594.8 ± 10.7
.0123	550.9 ± 10.8	565.6 ± 10.4
.0130	540.5 ± 10.7	557.0 ± 10.3
.0138	557.8 ± 10.9	542.1 ± 10.2
.0145	539.8 ± 10.7	527.8 ± 10.0
.0153	512.8 ± 10.5	530.2 ± 10.0
.0160	492.1 ± 10.2	521.7 ± 10.0
.0168	500.6 ± 10.3	491.7 ± 9.7
.0175	483.7 ± 10.2	489.5 ± 9.6
.0183	468.1 ± 10.0	462.5 ± 9.4
.0190	454.1 ± 9.8	466.9 ± 9.4
.0198	420.2 ± 9.5	459.6 ± 9.3
.0205	428.7 ± 9.6	423.2 + 9.0
.0212	428.5 ± 9.6	425.2 ± 9.0
.0220	398.2 ± 9.2	418.2 ± 8.9
.0227	401.4 ± 9.2	394.6 ± 8.7
.0235	379.5 ± 9.0	393.2 ± 8.6
.0242	381.3 ± 9.0	383.0 ± 8.5
.0250	363.8 ± 8.8	361.9 ± 8.3
.0257	358.3 ± 8.7	365.8 ± 8.3
.0265	350.2 ± 8.6	332.3 ± 7.9
.0272	338.2 ± 8.5	346.5 ± 8.1
.0280	326.4 ± 8.3	325.4 ± 7.9
.0287	320.9 ± 8.3	317.2 ± 7.8
.0294	301.1 ± 8.0	313.4 ± 7.7
.0302	298.5 ± 8.0	312.6 ± 7.7
.0309	294.1 ± 7.9	297.1 ± 7.5
.0317	296.9 ± 8.0	296.9 ± 7.5
.0324	267.3 ± 7.5	297.2 ± 7.5
.0332	274.7 ± 7.7	271.9 ± 7.2
.0339	270.1 ± 7.6	266.8 ± 7.1
.0347	269.0 ± 7.6	257.4 ± 7.0
.0354	261.3 ± 7.5	256.3 ± 7.0
.0362	248.0 ± 7.3	249.6 ± 6.9
.0369	246.9 ± 7.3	245.5 ± 6.8
.0376	244.9 ± 7.2	237.6 ± 6.7
.0384	234.6 ± 7.1	229.2 ± 6.6
.0391	224.0 ± 6.9	224.4 ± 6.5
.0399	229.0 ± 7.0	218.3 ± 6.4
.0406	214.4 ± 6.8	215.5 ± 6.4
.0414	212.0 ± 6.7	207.6 ± 6.3
.0421	205.8 ± 6.6	200.4 ± 6.2
.0429	207.6 ± 6.7	208.1 ± 6.3
.0436	188.3 ± 6.3	196.1 ± 6.1
.0444	192.4 ± 6.4	183.6 ± 5.9
.0451	180.6 ± 6.2	181.3 ± 5.9
.0458	178.3 ± 6.2	163.7 ± 5.6
.0466	184.7 ± 6.3	172.4 ± 5.7
.0473	162.7 ± 5.9	179.2 ± 5.8
.0481	167.5 ± 6.0	161.0 ± 5.5

P-HE +100 GEV +150 GEV

TABLE II
(continued)

T GEV**2	CROSS SECTION MB/(GEV**2)	CROSS SECTION MB/(GEV**2)
.0078	686.1 ± 10.3	680.8 ± 9.6
.0086	648.7 ± 9.8	672.9 ± 9.4
.0093	650.5 ± 9.8	637.8 ± 9.1
.0101	633.1 ± 9.7	643.5 ± 9.1
.0108	633.3 ± 9.7	618.4 ± 8.9
.0116	597.3 ± 9.4	607.5 ± 8.8
.0123	579.9 ± 9.2	573.8 ± 8.6
.0130	570.7 ± 9.2	571.7 ± 8.6
.0138	543.6 ± 8.9	543.2 ± 8.3
.0145	535.7 ± 8.9	541.3 ± 8.3
.0153	530.1 ± 8.8	530.3 ± 8.2
.0160	517.0 ± 8.7	507.0 ± 8.0
.0168	492.3 ± 8.5	489.5 ± 7.9
.0175	489.4 ± 8.5	475.3 ± 7.8
.0183	478.4 ± 8.4	467.4 ± 7.7
.0190	459.7 ± 8.2	458.8 ± 7.7
.0198	446.1 ± 8.1	453.2 ± 7.6
.0205	437.0 ± 8.0	442.7 ± 7.5
.0212	425.2 ± 7.9	422.2 ± 7.3
.0220	421.3 ± 7.9	424.0 ± 7.4
.0227	405.9 ± 7.7	396.5 ± 7.1
.0235	404.5 ± 7.7	385.1 ± 7.0
.0242	387.6 ± 7.5	380.0 ± 7.0
.0250	366.9 ± 7.3	374.7 ± 6.9
.0257	372.8 ± 7.4	357.3 ± 6.8
.0265	350.0 ± 7.2	350.6 ± 6.7
.0272	351.8 ± 7.2	344.3 ± 6.6
.0280	333.0 ± 7.0	321.7 ± 6.4
.0287	335.4 ± 7.0	338.0 ± 6.6
.0294	321.8 ± 6.9	328.8 ± 6.5
.0302	313.6 ± 6.8	302.2 ± 6.2
.0309	305.0 ± 6.7	308.9 ± 6.3
.0317	293.2 ± 6.6	297.7 ± 6.2
.0324	283.9 ± 6.4	279.9 ± 6.0
.0332	269.6 ± 6.3	274.9 ± 5.9
.0339	276.1 ± 6.4	273.2 ± 5.9
.0347	270.4 ± 6.3	270.4 ± 5.9
.0354	263.3 ± 6.2	261.2 ± 5.8
.0362	255.2 ± 6.1	257.8 ± 5.7
.0369	260.4 ± 6.2	248.5 ± 5.6
.0376	241.9 ± 6.0	250.2 ± 5.6
.0384	228.8 ± 5.8	236.3 ± 5.5
.0391	235.4 ± 5.9	221.4 ± 5.3
.0399	222.1 ± 5.7	226.2 ± 5.4
.0406	217.4 ± 5.6	211.4 ± 5.2
.0414	216.0 ± 5.6	197.3 ± 5.0
.0421	215.4 ± 5.6	204.1 ± 5.1
.0429	196.4 ± 5.4	185.6 ± 4.9
.0436	196.1 ± 5.4	193.7 ± 5.0
.0444	189.3 ± 5.3	185.6 ± 4.9
.0451	175.8 ± 5.1	193.1 ± 5.0
.0458	174.9 ± 5.1	173.4 ± 4.7
.0466	174.5 ± 5.1	176.7 ± 4.7
.0473	170.2 ± 5.0	165.1 ± 4.6
.0481	162.1 ± 4.9	160.9 ± 4.5

P-HE +250 GEV +300 GEV

TABLE II
(continued)

T GEV**2	CROSS SECTION MB/(GEV**2)	CROSS SECTION MB/(GEV**2)	CROSS SECTION MB/(GEV**2)
.0078		277.6 ± 12.2	300.1 ± 5.7
.0086		277.3 ± 11.9	294.4 ± 5.6
.0093		273.7 ± 11.6	286.2 ± 5.5
.0101		293.9 ± 11.9	280.1 ± 5.4
.0108	252.8 ± 5.6	249.8 ± 10.8	281.0 ± 5.4
.0116	262.1 ± 5.7	243.2 ± 10.6	273.4 ± 5.4
.0123	256.5 ± 5.7	233.2 ± 10.4	251.7 ± 5.1
.0130	233.9 ± 5.4	224.4 ± 10.2	244.8 ± 5.1
.0138	234.4 ± 5.4	230.4 ± 10.3	248.2 ± 5.1
.0145	223.1 ± 5.3	232.8 ± 10.3	234.4 ± 5.0
.0153	223.5 ± 5.3	224.5 ± 10.2	234.2 ± 5.0
.0160	227.8 ± 5.4	219.4 ± 10.0	222.8 ± 4.8
.0168	210.8 ± 5.2	213.6 ± 9.9	218.0 ± 4.8
.0175	209.8 ± 5.1	201.9 ± 9.6	221.2 ± 4.8
.0183	208.8 ± 5.1	204.2 ± 9.7	209.4 ± 4.7
.0190	202.1 ± 5.0	185.4 ± 9.2	209.2 ± 4.7
.0198	200.0 ± 5.0	193.7 ± 9.4	202.0 ± 4.6
.0205	183.7 ± 4.8	191.5 ± 9.4	192.3 ± 4.5
.0212	192.2 ± 4.9	179.6 ± 9.1	184.5 ± 4.4
.0220	182.7 ± 4.8	196.1 ± 9.5	183.9 ± 4.4
.0227	179.2 ± 4.8	163.9 ± 8.7	180.7 ± 4.3
.0235	159.8 ± 4.5	177.3 ± 9.0	175.7 ± 4.3
.0242	168.3 ± 4.6	159.8 ± 8.6	175.1 ± 4.3
.0250	171.2 ± 4.6	164.5 ± 8.7	170.2 ± 4.2
.0257	160.0 ± 4.5	167.3 ± 8.8	163.3 ± 4.1
.0265	156.0 ± 4.4	153.4 ± 8.4	151.1 ± 4.0
.0272	157.4 ± 4.5	157.3 ± 8.5	153.1 ± 4.0
.0280	151.7 ± 4.4	151.3 ± 8.3	148.0 ± 3.9
.0287	150.2 ± 4.4	141.2 ± 8.1	150.3 ± 4.0
.0294	144.2 ± 4.3	138.3 ± 8.0	150.2 ± 4.0
.0302	143.0 ± 4.3	123.2 ± 7.5	138.7 ± 3.8
.0309	133.6 ± 4.1	139.8 ± 8.0	135.6 ± 3.8
.0317	129.4 ± 4.0	138.5 ± 8.0	136.3 ± 3.8
.0324	126.8 ± 4.0	134.3 ± 7.9	129.3 ± 3.7
.0332	128.0 ± 4.0	133.9 ± 7.8	132.7 ± 3.7
.0339	124.7 ± 4.0	124.7 ± 7.6	130.8 ± 3.7
.0347	119.7 ± 3.9	127.5 ± 7.7	123.4 ± 3.6
.0354	115.1 ± 3.8	114.1 ± 7.2	124.7 ± 3.6
.0362	111.5 ± 3.8	109.6 ± 7.1	125.7 ± 3.6
.0369	117.5 ± 3.9	109.6 ± 7.1	115.9 ± 3.5
.0376	104.5 ± 3.6	113.3 ± 7.2	114.9 ± 3.5
.0384	103.9 ± 3.6	114.2 ± 7.3	110.3 ± 3.4
.0391	102.9 ± 3.6	109.1 ± 7.1	106.4 ± 3.3
.0399	102.5 ± 3.6	100.4 ± 6.8	109.1 ± 3.4
.0406	99.4 ± 3.5	98.1 ± 6.7	105.2 ± 3.3
.0414	97.3 ± 3.5	100.4 ± 6.8	99.7 ± 3.2
.0421	92.2 ± 3.4	103.7 ± 6.9	95.7 ± 3.2
.0429	89.7 ± 3.4	84.3 ± 6.2	98.2 ± 3.2
.0436	90.9 ± 3.4	87.6 ± 6.4	91.5 ± 3.1
.0444	90.8 ± 3.4	85.7 ± 6.3	92.2 ± 3.1
.0451	90.5 ± 3.4	89.9 ± 6.4	93.9 ± 3.1
.0458	88.6 ± 3.3	79.7 ± 6.1	83.0 ± 3.0
.0466	86.5 ± 3.3	79.3 ± 6.0	86.8 ± 3.0
.0473	80.9 ± 3.2	94.1 ± 6.6	87.5 ± 3.0
.0481	76.8 ± 3.1		80.3 ± 2.9

TABLE II
(continued)

T GEV**2	CROSS SECTION MB/(GEV**2)	CROSS SECTION MB/(GEV**2)	CROSS SECTION MB/(GEV**2)
.0078	306.2 ± 4.7	———	310.3 ± 4.7
.0086	292.9 ± 4.5	288.3 ± 7.7	307.8 ± 4.6
.0093	288.9 ± 4.5	289.0 ± 7.4	294.0 ± 4.5
.0101	283.9 ± 4.4	284.8 ± 7.3	288.4 ± 4.5
.0108	284.0 ± 4.4	302.0 ± 7.4	287.5 ± 4.5
.0116	264.3 ± 4.2	288.2 ± 7.1	270.1 ± 4.3
.0123	263.3 ± 4.2	261.7 ± 6.8	265.0 ± 4.3
.0130	258.0 ± 4.2	253.9 ± 6.7	262.2 ± 4.3
.0138	243.7 ± 4.1	256.2 ± 6.7	251.7 ± 4.2
.0145	241.8 ± 4.1	244.2 ± 6.5	253.3 ± 4.2
.0153	237.5 ± 4.0	248.9 ± 6.6	233.7 ± 4.0
.0160	232.5 ± 4.0	234.7 ± 6.4	234.9 ± 4.0
.0168	225.9 ± 3.9	231.7 ± 6.3	226.0 ± 4.0
.0175	219.4 ± 3.9	216.9 ± 6.1	233.0 ± 4.0
.0183	209.5 ± 3.8	218.7 ± 6.2	213.6 ± 3.8
.0190	208.1 ± 3.8	198.7 ± 5.9	213.5 ± 3.8
.0198	199.5 ± 3.7	208.0 ± 6.0	209.8 ± 3.8
.0205	198.4 ± 3.7	199.3 ± 5.9	197.8 ± 3.7
.0212	191.5 ± 3.6	193.1 ± 5.8	194.9 ± 3.7
.0220	190.1 ± 3.6	196.5 ± 5.8	190.6 ± 3.6
.0227	183.7 ± 3.5	186.2 ± 5.7	191.6 ± 3.6
.0235	185.1 ± 3.5	179.7 ± 5.6	179.3 ± 3.5
.0242	174.0 ± 3.4	178.4 ± 5.6	182.3 ± 3.5
.0250	175.9 ± 3.5	175.5 ± 5.5	178.9 ± 3.5
.0257	169.2 ± 3.4	170.7 ± 5.4	161.7 ± 3.3
.0265	159.5 ± 3.3	154.1 ± 5.2	167.7 ± 3.4
.0272	153.9 ± 3.2	157.8 ± 5.2	157.8 ± 3.3
.0280	160.3 ± 3.3	157.5 ± 5.2	161.3 ± 3.3
.0287	153.2 ± 3.2	149.5 ± 5.1	155.4 ± 3.3
.0294	148.9 ± 3.2	140.9 ± 4.9	160.6 ± 3.3
.0302	148.7 ± 3.2	141.3 ± 5.0	148.6 ± 3.2
.0309	138.3 ± 3.1	150.8 ± 5.1	147.7 ± 3.2
.0317	135.9 ± 3.0	128.3 ± 4.7	143.6 ± 3.2
.0324	134.0 ± 3.0	140.7 ± 4.9	134.9 ± 3.1
.0332	132.8 ± 3.0	128.4 ± 4.7	137.7 ± 3.1
.0339	133.4 ± 3.0	135.5 ± 4.9	136.0 ± 3.1
.0347	128.8 ± 3.0	124.7 ± 4.7	129.9 ± 3.0
.0354	124.4 ± 2.9	124.1 ± 4.6	130.8 ± 3.0
.0362	121.5 ± 2.9	112.3 ± 4.4	119.3 ± 2.9
.0369	119.4 ± 2.9	122.9 ± 4.6	116.3 ± 2.8
.0376	116.0 ± 2.8	113.5 ± 4.4	111.5 ± 2.8
.0384	111.6 ± 2.8	120.0 ± 4.6	110.1 ± 2.8
.0391	109.7 ± 2.7	117.3 ± 4.5	106.4 ± 2.7
.0399	105.6 ± 2.7	105.0 ± 4.3	108.7 ± 2.7
.0406	105.1 ± 2.7	99.0 ± 4.2	102.5 ± 2.7
.0414	100.2 ± 2.6	102.9 ± 4.2	100.0 ± 2.6
.0421	97.9 ± 2.6	103.1 ± 4.2	98.6 ± 2.6
.0429	96.5 ± 2.6	96.4 ± 4.1	101.3 ± 2.6
.0436	91.2 ± 2.5	96.2 ± 4.1	96.3 ± 2.6
.0444	91.6 ± 2.5	96.1 ± 4.1	92.8 ± 2.5
.0451	94.0 ± 2.5	87.3 ± 3.9	93.5 ± 2.5
.0458	91.3 ± 2.5	87.9 ± 3.9	94.2 ± 2.6
.0466	86.6 ± 2.4	81.2 ± 3.8	88.2 ± 2.5
.0473	84.5 ± 2.4	85.2 ± 3.9	86.7 ± 2.5
.0481	80.3 ± 2.3	84.5 ± 3.8	80.0 ± 2.4

PI-HE -250 GEV -280 GEV -300 GEV

TABLE II
(continued)

T GEV**2	CROSS SECTION MB/(GEV**2)	CROSS SECTION MB/(GEV**2)
.0078		291.5 ± 8.7
.0086		282.8 ± 8.5
.0093		271.2 ± 8.3
.0101		278.5 ± 8.4
.0108	257.5 ± 5.6	258.0 ± 8.1
.0116	264.5 ± 5.7	252.8 ± 8.0
.0123	239.8 ± 5.5	248.5 ± 7.9
.0130	239.7 ± 5.5	253.4 ± 8.0
.0138	247.2 ± 5.5	245.9 ± 7.8
.0145	231.5 ± 5.4	230.0 ± 7.6
.0153	222.9 ± 5.3	250.4 ± 7.9
.0160	222.8 ± 5.3	231.4 ± 7.6
.0168	213.7 ± 5.1	221.2 ± 7.4
.0175	209.6 ± 5.1	223.8 ± 7.5
.0183	197.2 ± 4.9	201.0 ± 7.1
.0190	195.5 ± 4.9	199.4 ± 7.1
.0198	189.5 ± 4.9	199.3 ± 7.1
.0205	193.7 ± 4.9	176.8 ± 6.6
.0212	187.9 ± 4.8	194.5 ± 7.0
.0220	176.3 ± 4.7	188.9 ± 6.9
.0227	174.6 ± 4.7	182.2 ± 6.7
.0235	173.2 ± 4.6	178.0 ± 6.7
.0242	165.6 ± 4.5	163.1 ± 6.4
.0250	177.6 ± 4.7	161.8 ± 6.4
.0257	158.9 ± 4.4	158.6 ± 6.3
.0265	158.4 ± 4.4	161.6 ± 6.4
.0272	149.7 ± 4.3	154.3 ± 6.2
.0280	149.8 ± 4.3	147.9 ± 6.1
.0287	147.8 ± 4.3	152.3 ± 6.2
.0294	140.5 ± 4.2	146.7 ± 6.1
.0302	139.6 ± 4.2	135.4 ± 5.8
.0309	131.7 ± 4.0	129.3 ± 5.7
.0317	130.5 ± 4.0	139.8 ± 5.9
.0324	130.2 ± 4.0	130.4 ± 5.7
.0332	129.3 ± 4.0	120.8 ± 5.5
.0339	114.3 ± 3.8	126.4 ± 5.6
.0347	121.2 ± 3.9	119.8 ± 5.5
.0354	110.9 ± 3.7	122.1 ± 5.5
.0362	116.7 ± 3.8	114.5 ± 5.4
.0369	108.1 ± 3.7	121.4 ± 5.5
.0376	113.4 ± 3.8	110.4 ± 5.3
.0384	105.0 ± 3.6	103.8 ± 5.1
.0391	96.8 ± 3.5	111.2 ± 5.3
.0399	106.4 ± 3.6	104.1 ± 5.1
.0406	104.1 ± 3.6	96.6 ± 4.9
.0414	103.9 ± 3.6	91.5 ± 4.8
.0421	98.6 ± 3.5	97.9 ± 5.0
.0429	97.9 ± 3.5	100.7 ± 5.0
.0436	88.0 ± 3.3	90.0 ± 4.7
.0444	81.3 ± 3.2	85.6 ± 4.6
.0451	87.5 ± 3.3	86.9 ± 4.7
.0458	88.0 ± 3.3	81.3 ± 4.5
.0466	84.5 ± 3.2	86.0 ± 4.6
.0473	78.6 ± 3.1	85.5 ± 4.6
.0481	81.9 ± 3.2	77.5 ± 4.4

PI-HE +100 GEV +150 GEV

TABLE II
(continued)

T GEV**2	CROSS SECTION MB/(GEV**2)	CROSS SECTION MB/(GEV**2)	CROSS SECTION MB/(GEV**2)
.0086	283.3 ± 5.7	276.3 ± 9.6	285.2 ± 8.6
.0093	283.2 ± 5.7	260.1 ± 9.3	264.0 ± 8.3
.0101	253.2 ± 5.4	288.6 ± 9.8	266.7 ± 8.3
.0108	263.1 ± 5.5	256.4 ± 9.2	264.5 ± 8.3
.0116	258.2 ± 5.4	260.4 ± 9.3	245.3 ± 8.0
.0123	250.3 ± 5.3	243.0 ± 9.0	237.9 ± 7.8
.0130	250.1 ± 5.3	240.0 ± 8.9	250.8 ± 8.1
.0138	238.6 ± 5.2	229.9 ± 8.7	239.0 ± 7.9
.0145	242.5 ± 5.3	234.6 ± 8.8	229.0 ± 7.7
.0153	219.8 ± 5.0	226.0 ± 8.7	224.3 ± 7.6
.0160	232.8 ± 5.1	217.0 ± 8.5	226.3 ± 7.7
.0168	219.2 ± 5.0	225.8 ± 8.7	216.0 ± 7.5
.0175	204.9 ± 4.8	222.3 ± 8.6	226.5 ± 7.7
.0183	208.0 ± 4.9	208.0 ± 8.3	192.6 ± 7.1
.0190	201.4 ± 4.8	206.5 ± 8.3	194.9 ± 7.1
.0198	184.2 ± 4.6	194.5 ± 8.1	195.3 ± 7.1
.0205	192.3 ± 4.7	201.1 ± 8.2	185.1 ± 6.9
.0212	193.6 ± 4.7	196.1 ± 8.1	189.3 ± 7.0
.0220	189.9 ± 4.7	185.7 ± 7.9	191.9 ± 7.1
.0227	186.6 ± 4.6	164.9 ± 7.4	167.4 ± 6.6
.0235	180.5 ± 4.5	184.7 ± 7.9	163.6 ± 6.5
.0242	178.4 ± 4.5	179.6 ± 7.7	155.3 ± 6.4
.0250	171.5 ± 4.4	168.9 ± 7.5	161.5 ± 6.5
.0257	169.6 ± 4.4	150.0 ± 7.1	160.0 ± 6.5
.0265	164.4 ± 4.3	147.6 ± 7.0	147.8 ± 6.2
.0272	166.0 ± 4.4	156.0 ± 7.2	155.5 ± 6.4
.0280	156.9 ± 4.2	150.9 ± 7.1	150.5 ± 6.3
.0287	148.2 ± 4.1	148.2 ± 7.0	146.9 ± 6.2
.0294	150.0 ± 4.1	146.6 ± 7.0	145.4 ± 6.2
.0302	141.7 ± 4.0	133.1 ± 6.7	133.6 ± 5.9
.0309	152.1 ± 4.2	121.9 ± 6.4	138.1 ± 6.0
.0317	137.5 ± 4.0	134.3 ± 6.7	127.1 ± 5.8
.0324	124.6 ± 3.8	128.8 ± 6.6	125.7 ± 5.7
.0332	130.5 ± 3.9	134.9 ± 6.7	133.7 ± 5.9
.0339	124.3 ± 3.8	114.9 ± 6.2	128.7 ± 5.8
.0347	128.8 ± 3.8	131.4 ± 6.6	124.2 ± 5.7
.0354	115.9 ± 3.6	136.5 ± 6.8	121.3 ± 5.6
.0362	118.2 ± 3.7	115.0 ± 6.2	110.5 ± 5.4
.0369	109.0 ± 3.5	118.3 ± 6.3	126.2 ± 5.7
.0376	111.5 ± 3.6	131.1 ± 6.6	113.1 ± 5.4
.0384	110.1 ± 3.6	114.0 ± 6.2	108.7 ± 5.3
.0391	106.8 ± 3.5	98.0 ± 5.7	108.0 ± 5.3
.0399	103.2 ± 3.4	111.2 ± 6.1	103.9 ± 5.2
.0406	104.7 ± 3.5	104.1 ± 5.9	97.5 ± 5.1
.0414	97.1 ± 3.3	99.7 ± 5.8	104.9 ± 5.2
.0421	95.7 ± 3.3	102.6 ± 5.9	100.3 ± 5.1
.0429	96.6 ± 3.3	104.6 ± 5.9	94.6 ± 5.0
.0436	95.0 ± 3.3	91.4 ± 5.6	92.0 ± 4.9
.0444	89.3 ± 3.2	97.8 ± 5.7	103.7 ± 5.2

PI-HE -50 GEV -80 GEV -100 GEV

TABLE II
(continued)

T GEV**2	CROSS SECTION MB/(GEV**2)	CROSS SECTION MB/(GEV**2)
.0086	271.1 ± 8.9	273.1 ± 8.6
.0093	287.6 ± 9.2	286.6 ± 8.8
.0101	276.1 ± 9.0	280.1 ± 8.7
.0108	270.5 ± 8.9	260.3 ± 8.4
.0116	249.9 ± 8.6	262.9 ± 8.4
.0123	254.1 ± 8.7	243.7 ± 8.1
.0130	250.2 ± 8.6	239.4 ± 8.1
.0138	243.1 ± 8.5	245.0 ± 8.1
.0145	223.8 ± 8.1	238.6 ± 8.0
.0153	230.6 ± 8.3	229.9 ± 7.9
.0160	220.8 ± 8.1	208.0 ± 7.5
.0168	233.4 ± 8.3	196.6 ± 7.3
.0175	202.1 ± 7.7	205.7 ± 7.5
.0183	201.6 ± 7.7	198.7 ± 7.3
.0190	204.5 ± 7.8	195.2 ± 7.3
.0198	184.2 ± 7.4	196.6 ± 7.3
.0205	175.9 ± 7.2	179.4 ± 7.0
.0212	189.9 ± 7.5	186.9 ± 7.1
.0220	187.8 ± 7.5	180.6 ± 7.0
.0227	191.7 ± 7.5	183.9 ± 7.1
.0235	184.4 ± 7.4	171.6 ± 6.8
.0242	187.0 ± 7.4	163.6 ± 6.7
.0250	168.2 ± 7.1	158.4 ± 6.6
.0257	171.2 ± 7.1	165.2 ± 6.7
.0265	155.1 ± 6.8	157.0 ± 6.5
.0272	140.2 ± 6.5	148.9 ± 6.4
.0280	149.7 ± 6.7	154.7 ± 6.5
.0287	147.7 ± 6.6	147.1 ± 6.3
.0294	148.3 ± 6.6	151.5 ± 6.4
.0302	134.9 ± 6.3	136.0 ± 6.1
.0309	151.3 ± 6.7	136.3 ± 6.1
.0317	122.4 ± 6.0	127.1 ± 5.9
.0324	132.1 ± 6.3	126.7 ± 5.9
.0332	133.7 ± 6.3	122.7 ± 5.8
.0339	120.8 ± 6.0	120.4 ± 5.7
.0347	125.7 ± 6.1	129.4 ± 6.0
.0354	131.4 ± 6.3	111.7 ± 5.5
.0362	104.3 ± 5.6	124.8 ± 5.8
.0369	116.5 ± 5.9	115.6 ± 5.6
.0376	110.1 ± 5.7	112.0 ± 5.5
.0384	100.7 ± 5.5	113.5 ± 5.6
.0391	110.8 ± 5.8	108.5 ± 5.5
.0399	109.4 ± 5.7	107.0 ± 5.4
.0406	118.9 ± 6.0	95.6 ± 5.1
.0414	104.9 ± 5.6	95.9 ± 5.1
.0421	97.5 ± 5.4	93.9 ± 5.1
.0429	94.8 ± 5.3	90.7 ± 5.0
.0436	81.7 ± 4.9	90.6 ± 5.0
.0444	88.4 ± 5.1	92.8 ± 5.0

PI-HE -120 GEV -140 GEV

TABLE III

Results from the phenomenological fit

Reaction	Energy GeV	b $(GeV)^{-2}$	σ_{tot} mb	χ^2/N	Statistics $\times 10^3$
(*) $\pi^- - {}^4He$	50	31.2 ± .4	84.6 ± .9	77/47	62
(*) "	80	30.1 ± .6	83.0 ± 1.1	65/47	24
(*) "	100	30.2 ± .6	82.5 ± 1.0	49/47	28
"	100	31.5 ± .4	83.7 ± .6	48/49	72
(*) "	120	31.1 ± .6	83.7 ± 1.1	77/47	26
(*) "	140	31.0 ± .6	82.9 ± 1.0	38/47	28
"	150	30.5 ± .7	83.0 ± .9	41/52	20
"	200	31.2 ± .3	84.1 ± .6	49/53	92
"	250	31.2 ± .2	84.7 ± .5	40/53	143
"	280	32.0 ± .4	85.8 ± .6	69/52	55
"	300	31.5 ± .2	85.6 ± .5	76/53	144
$\pi^+ - {}^4He$	100	31.7 ± .4	84.1 ± .6	63/49	75
"	150	32.3 ± .5	85.3 ± .7	47/53	38
$p - {}^4He$	100	34.1 ± .3	128.7 ± .9	46/49	98
"	150	34.9 ± .3	130.8 ± .8	47/53	111
"	250	34.7 ± .2	131.6 ± .8	42/53	145
"	300	35.1 ± .2	132.0 ± .8	63/53	166

(*) Results from the WA9 experiment

TABLE IV

Results from the Glauber fit

Reaction	Energy GeV	b_{hN} $(GeV)^{-2}$	K_2	σ_{tot} mb	χ^2/N	σ_{tot}^{GL} mb
(*) $\pi^- - {}^4He$	50	10.9 ± .5	1.09 ± .09	84.3 ± .9	75/47	85.0
(*) "	80	9.6 ± .8	1.18 ± .09	82.8 ± 1.1	65/47	84.9
(*) "	100	9.6 ± .7	1.24 ± .08	82.3 ± 1.0	50/47	85.1
"	100	10.9 ± .5	1.18 ± .05	83.4 ± .6	48/49	85.1
(*) "	120	10.6 ± .7	1.18 ± .09	83.5 ± 1.1	77/47	85.3
(*) "	140	10.2 ± .7	1.27 ± .09	82.8 ± 1.0	39/49	85.6
"	150	9.7 ± .8	1.27 ± .06	82.7 ± .9	41/52	85.8
"	200	10.5 ± .4	1.25 ± .04	84.0 ± .6	51/53	86.7
"	250	10.4 ± .4	1.27 ± .04	84.6 ± .5	39/53	87.6
"	280	11.1 ± .5	1.25 ± .05	85.5 ± .6	70/52	88.0
"	300	10.6 ± .3	1.26 ± .04	85.5 ± .5	75/53	88.3
$\pi^+ - {}^4He$	100	11.1 ± .5	1.15 ± .05	83.7 ± .6	64/49	85.1
"	150	11.8 ± .6	1.12 ± .06	84.9 ± .7	47/53	85.8
$p - {}^4He$	100	11.6 ± .4	1.12 ± .03	128.1 ± .9	49/49	131.3
"	150	12.7 ± .4	1.09 ± .03	130.2 ± .8	46/53	132.0
"	250	12.3 ± .3	1.10 ± .02	130.8 ± .8	39/53	133.5
"	300	12.6 ± .3	1.12 ± .02	131.2 ± .8	62/53	134.2

(*) Results from the WA9 experiment.

Figure captions

Fig. 1 : Lay-out of the experiment: B1-B8 are bending magnets; CED1, CED2 are differential Cerenkov counters; TH1, TH2 are threshold Cerenkov counters; BS1-BS4 are multiwire proportional chambers of the beam spectrometer; PC1-PC6 are blocks of multiwire proportional chambers; S1-S2, A1-A3 are scintillator counters; and IKAR is the recoil detector. In the beam lay-out all quadrupoles and correction dipoles and all collimators except the momentum-defining slit have been omitted.

Fig. 2 : The recoil detector IKAR. The upper picture shows schematically the construction of two cells of IKAR, and the diagram below shows the pulses produced on the electrodes by a recoil particle in the gas; d is the cathode-grid distance and W is the drift velocity of the electrons in the gas.

Fig. 3 : Plot showing the correlation between the recoil energy T_R and the length X_R of the recoil track projection on the beam axis for a sample of elastic events that have passed a preliminary selection.

Fig. 4 : Plot showing the correlation between the recoil energy T_R and the difference $\Delta = (p_0\theta)^2/2M_R - T_R$ between recoil energy for elastic events as measured by the forward spectrometer and as measured by the recoil detector, for a sample of events that have passed a preliminary selection.

Fig. 5 : The upper part of the figure shows the χ^2-distribution of the preliminary selected events (the solid line). The dashed line represents the test events normalized to the number of physical events in the region $\chi^2 < 15$. The relative amount of the test events beyond $\chi^2 = 15$ gives the number of good events rejected by the χ^2 cut (1.4%). The lower part of the figure shows the difference between physical and test events used to find the background under the χ^2 peak (0.7%).

Fig. 6 : Plot showing the momentum distribution of elastically scattered pions after the final selection of the elastic events.

Fig. 7 : Differential cross-sections for $p-^4He$ elastic scattering. The solid lines are the contribution to the cross-sections due to nuclear scattering taken in the form $d\sigma/dt = \frac{\sigma^2_{tot}}{16\hbar^2\pi}(1+\rho^2)\exp(bt)$. Also shown are the optical points: $\frac{d\sigma}{dt}(t=0) = \frac{\sigma^2_{tot}}{16\hbar^2\pi}$.

Fig. 8 : Same as Figure 7, but for π-He elastic scattering.

Fig. 9 : The inelastic shadowing corrections to the total $p-^4He$ and $\pi-^4He$ cross-sections $\Delta\sigma_{in} = \sigma^{Gl}_{tot} - \sigma_{tot}$.

Fig. 10 : Slope parameters from the phenomenological analysis of the $p-^4He$ and $\pi-^4He$ differential cross-sections.

Fig. 11 : Results from the fit to the $p-^4He$ differential cross-sections with the Glauber formula. K_2 is the factor increasing the double scattering term in the Glauber formula. b_{pN} is the elementary proton-nucleon slope parameter. For comparison, the results of a recent direct measurement of the pp slope parameter are indicated.

Fig. 12 : Results from the fit to the $\pi-^4He$ differential cross-sections with the Glauber formula. K_2 is the factor increasing the double scattering term in the Glauber formula. $b_{\pi N}$ is the elementary pion-nucleon slope parameter. For comparison, the results of two recent direct measurements of the πp slope parameter are indicated.

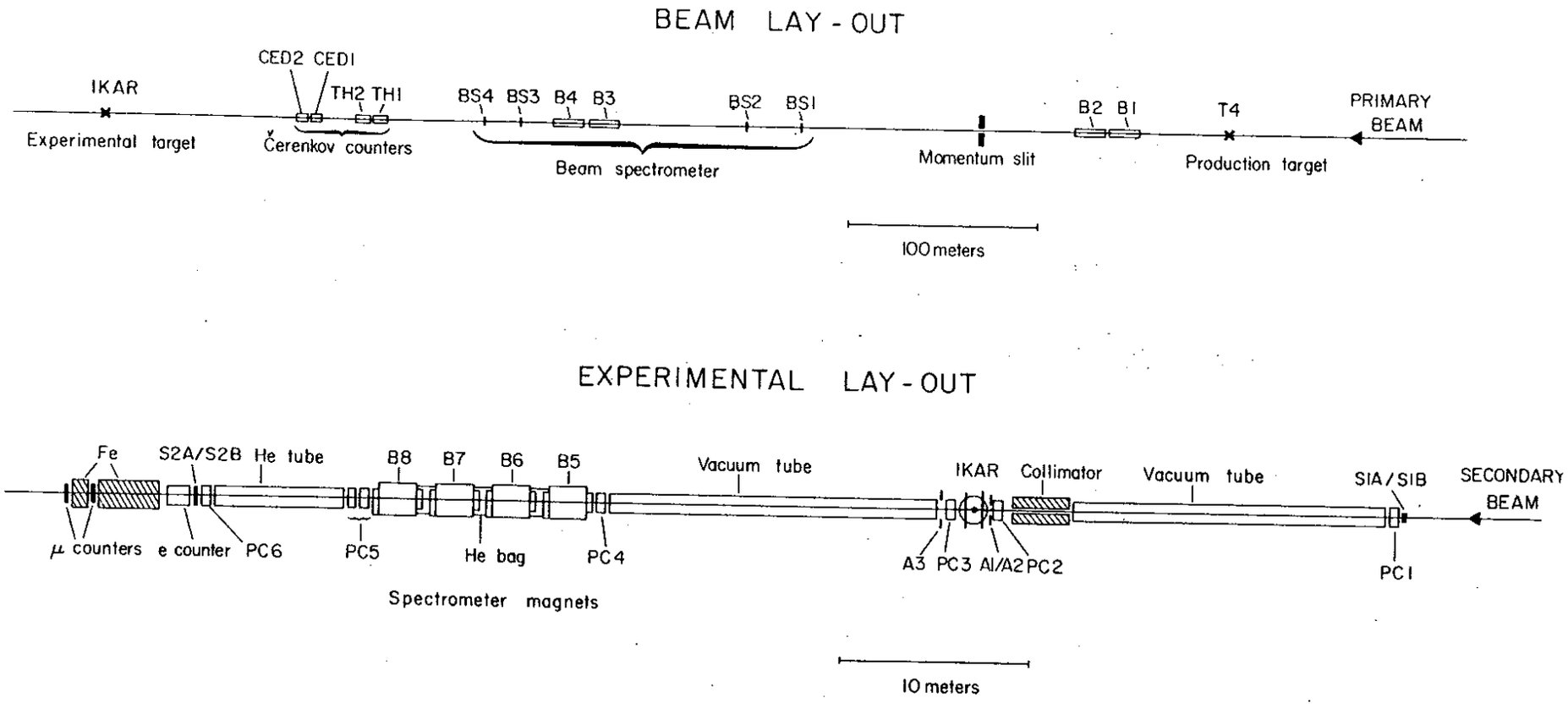
BEAM LAY-OUT
IKAR
Experimental target
CED2 CED1
TH2 TH1
Cerenkov counters
BS4 BS3 B4 B3
BS2 BS1
Beam spectrometer
Momentum slit
B2 B1
T4
Production target
PRIMARY BEAM
100 meters
EXPERIMENTAL LAY-OUT
Fe
S2A/S2B
He tube
B8 B7 B6 B5
Vacuum tube
IKAR
Collimator
Vacuum tube
SIA/SIB
SECONDARY BEAM
μ counters
e counter
PC6
PC5
He bag
PC4
A3 PC3 AI/A2 PC2
PC1
Spectrometer magnets
10 meters

Fig. 1

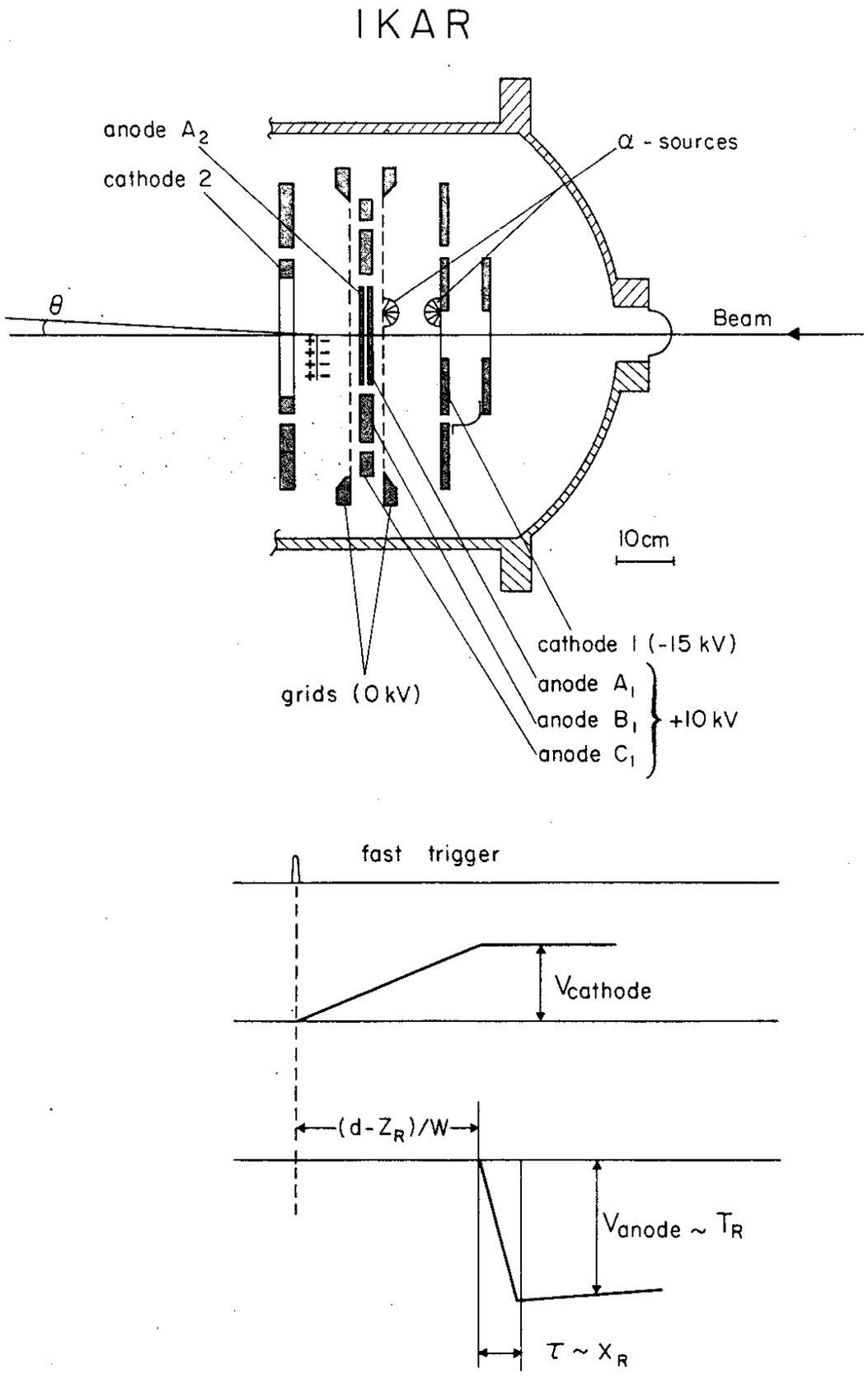
IKAR
anode A_2
cathode 2
α - sources
θ
Beam
10cm
cathode 1 (-15 kV)
grids (0 kV)
anode A_1
anode B_1
anode C_1
+10 kV
fast trigger
$V_{cathode}$
$(d-Z_R)/W$
$V_{anode} \sim T_R$
$\tau \sim X_R$

Fig. 2

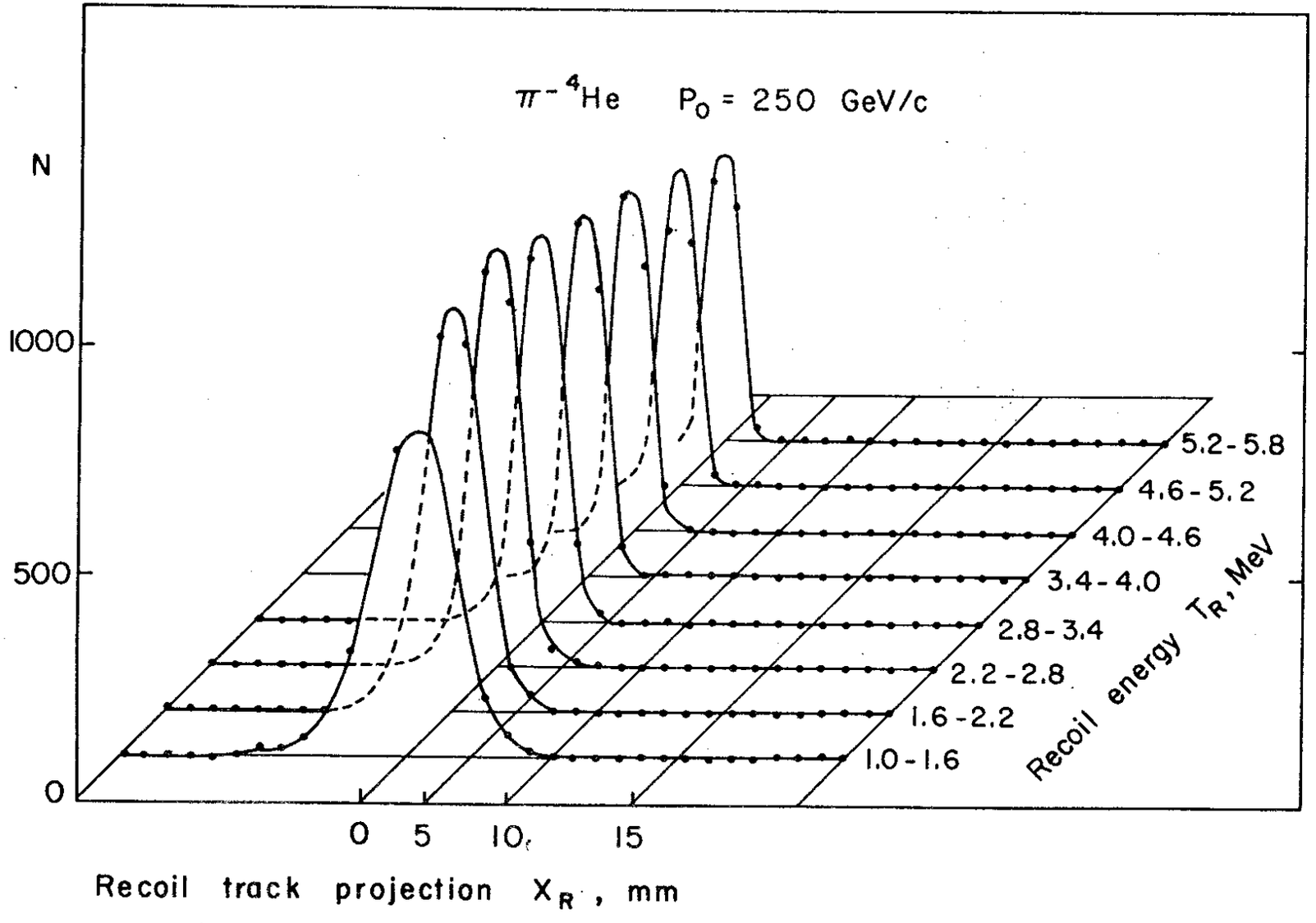
$\pi^- {}^4He$ P_0 = 250 GeV/c
N
1000
500
0
0
5
10
15
Recoil track projection X_R, mm
5.2-5.8
4.6-5.2
4.0-4.6
3.4-4.0
2.8-3.4
2.2-2.8
1.6-2.2
1.0-1.6
Recoil energy T_R, MeV

Fig. 3

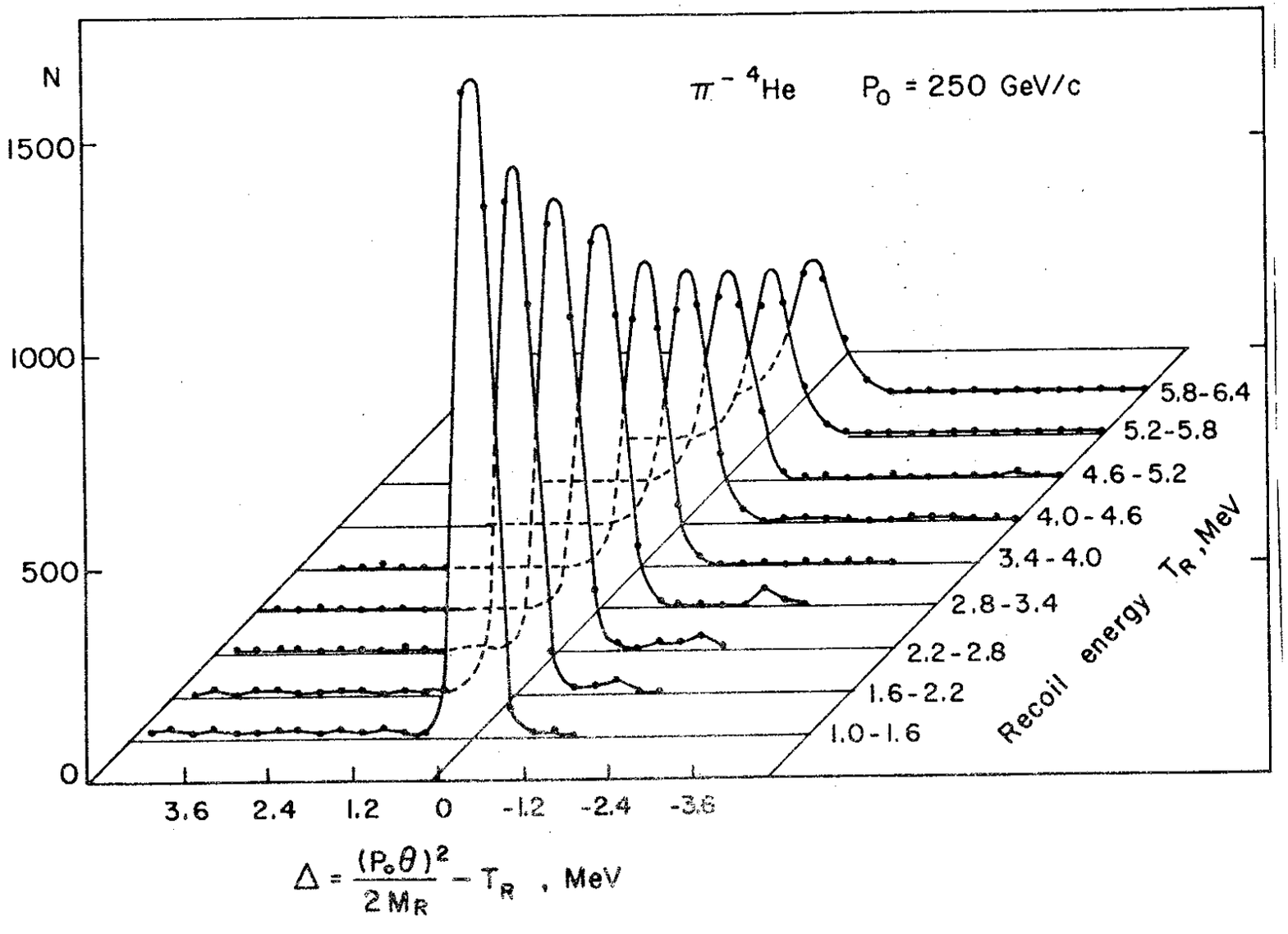
N
1500
1000
500
0
$\pi^- {}^4He$ P_0 = 250 GeV/c
5.8-6.4
5.2-5.8
4.6-5.2
4.0-4.6
3.4-4.0
2.8-3.4
2.2-2.8
1.6-2.2
1.0-1.6
Recoil energy T_R, MeV
3.6
2.4
1.2
0
-1.2
-2.4
-3.6
$\Delta = \frac{(P_0\theta)^2}{2M_R} - T_R$, MeV

Fig. 4

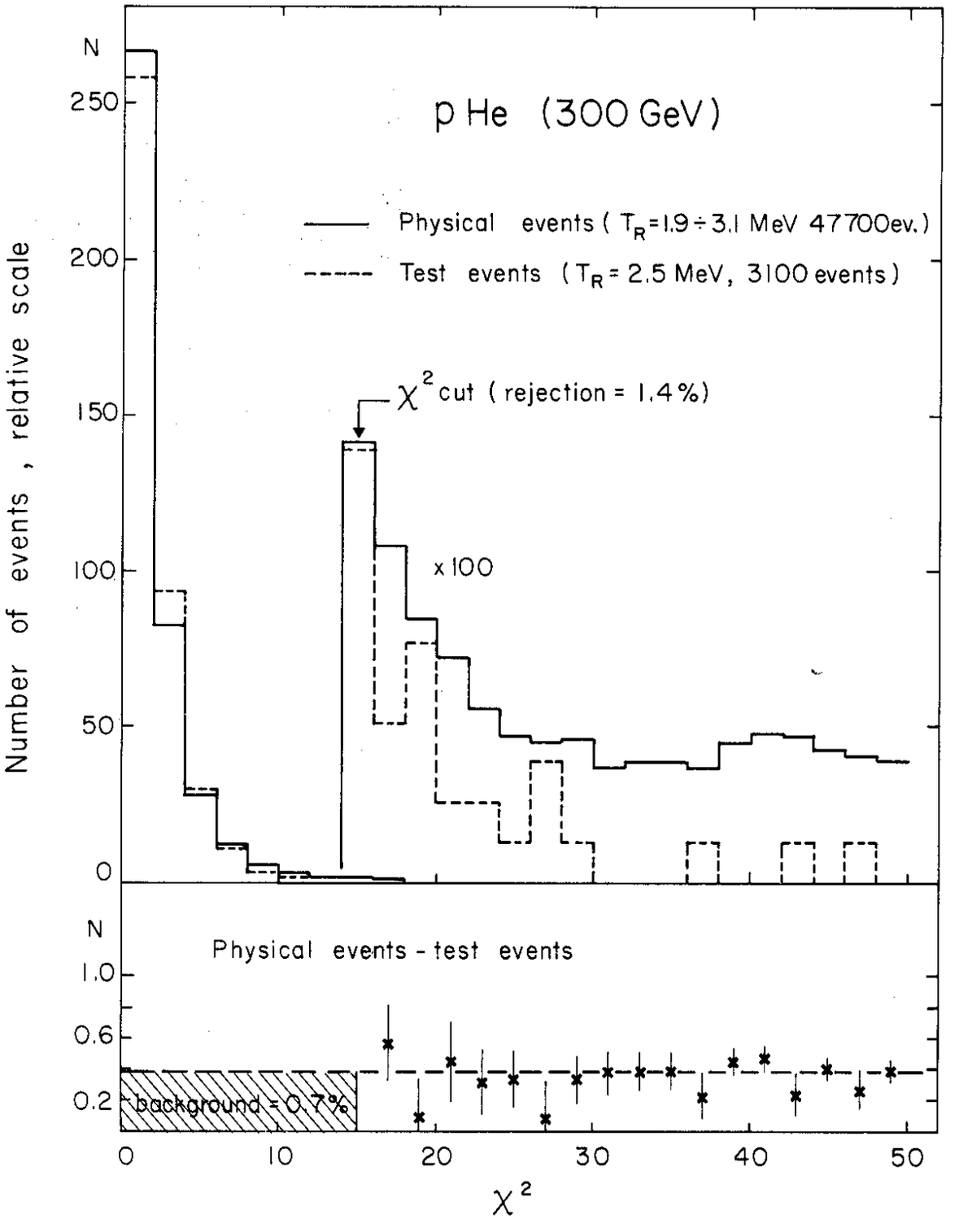
p He (300 GeV)
Physical events (T_R=1.9÷3.1 MeV 47700ev.)
Test events (T_R = 2.5 MeV, 3100 events)
χ^2 cut (rejection = 1.4%)
x 100
Number of events , relative scale
N
250
200
150
100
50
0
Physical events - test events
1.0
0.6
0.2
background = 0.7%
0
10
20
30
40
50
χ^2

Fig. 5

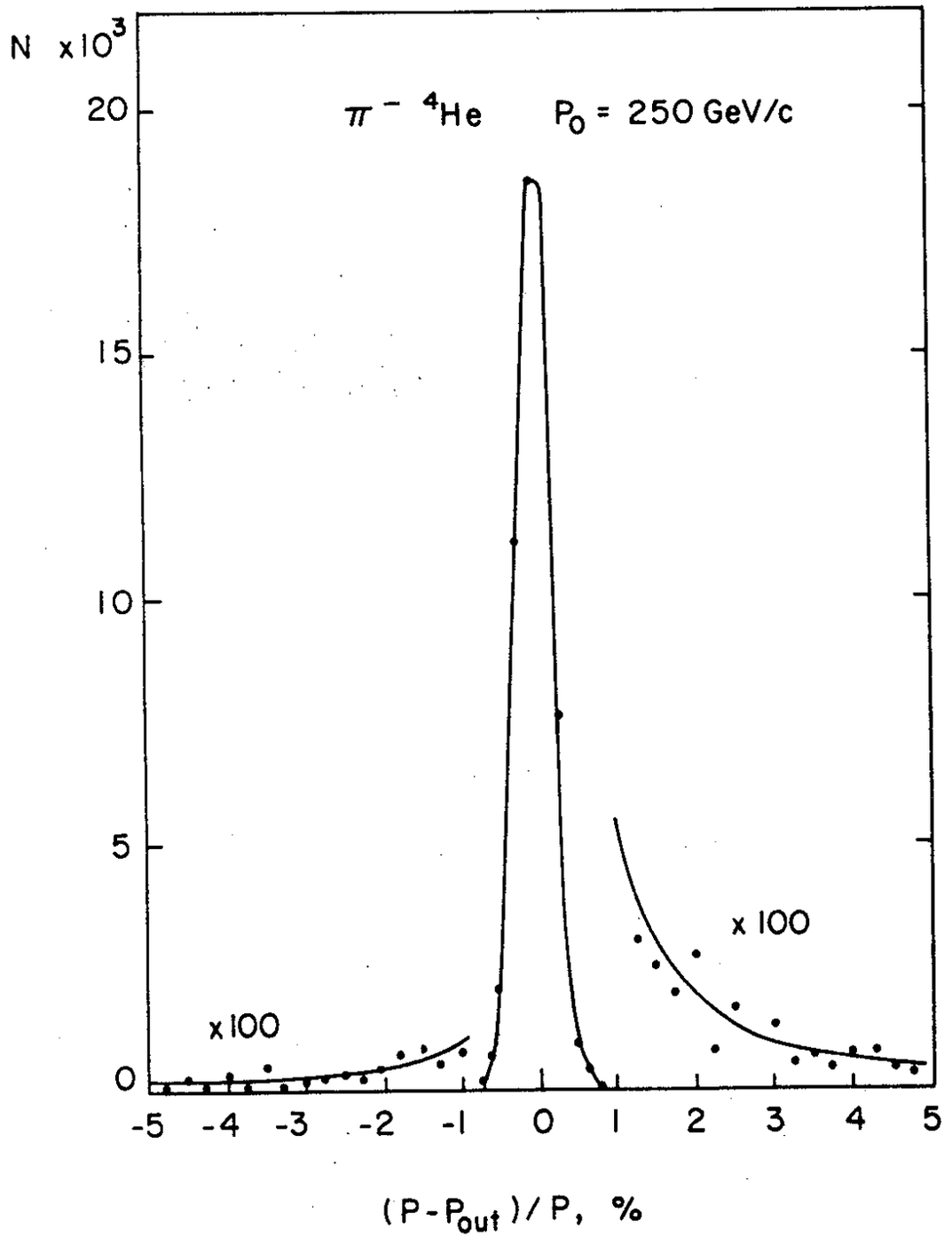
N x10^3
20
15
10
5
0
π⁻ ⁴He P₀ = 250 GeV/c
x100
x100
-5 -4 -3 -2 -1 0 1 2 3 4 5
(P-P_out)/P, %

Fig. 6

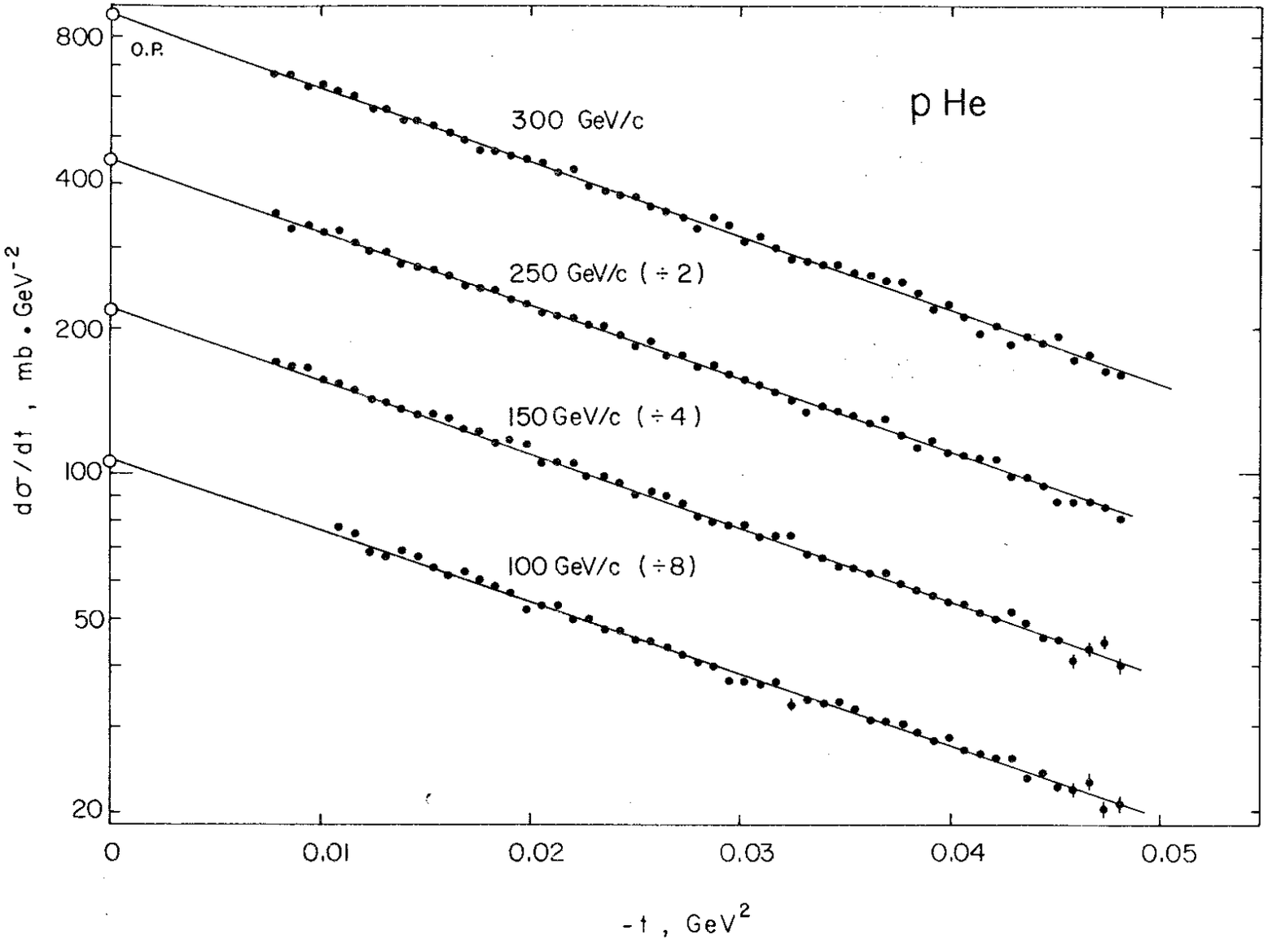
p He
300 GeV/c
250 GeV/c (÷2)
150 GeV/c (÷4)
100 GeV/c (÷8)
O.P.
800
400
200
100
50
20
0
0.01
0.02
0.03
0.04
0.05
dσ/dt , mb • GeV⁻²
-t , GeV²

Fig. 7

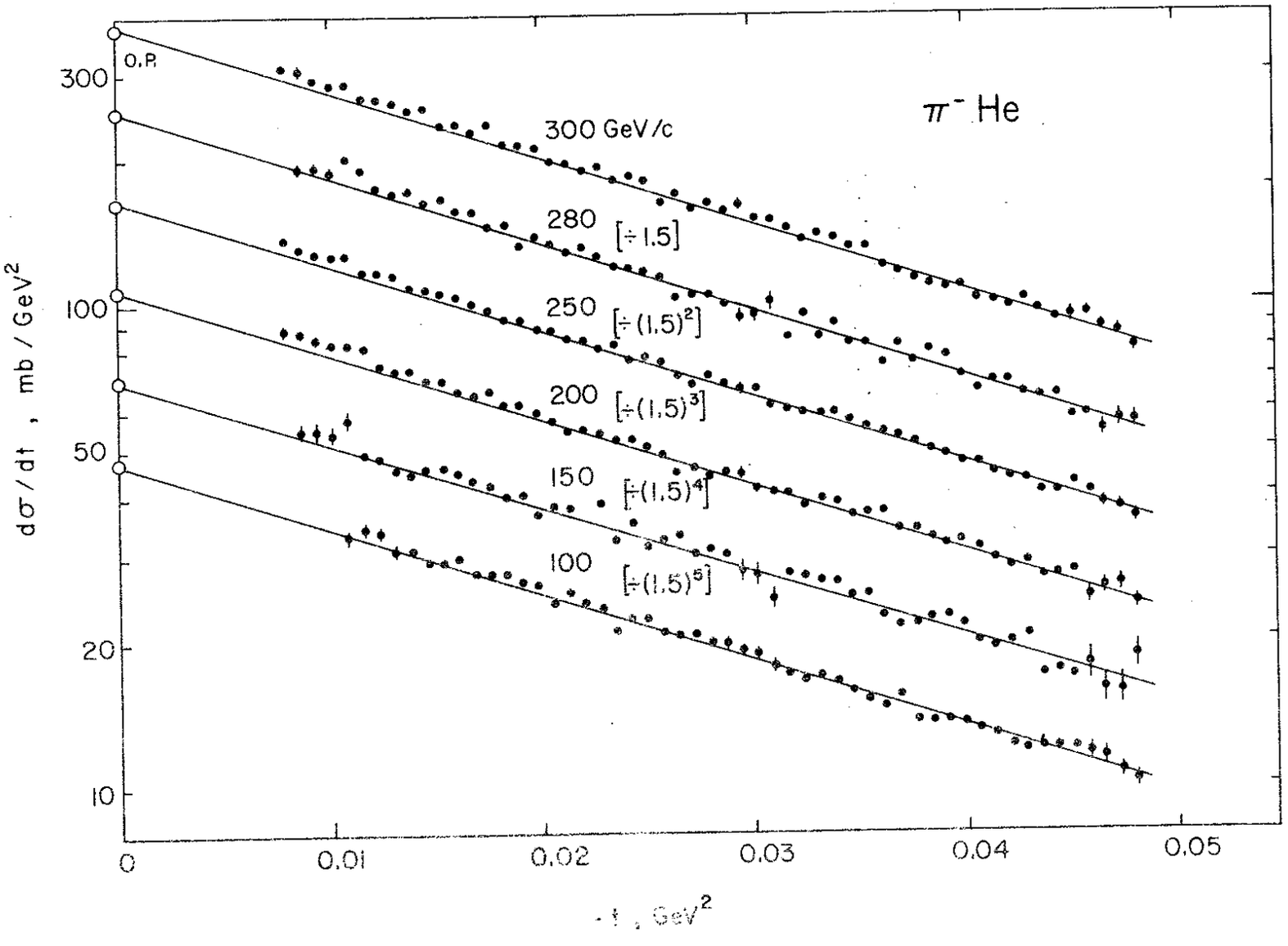
O.P.
300
100
50
20
10
π^- He
300 GeV/c
280 [÷1.5]
250 [÷(1.5)²]
200 [÷(1.5)³]
150 [÷(1.5)⁴]
100 [÷(1.5)⁵]
dσ/dt , mb / GeV²
0
0.01
0.02
0.03
0.04
0.05
-t , GeV²

Fig. 8

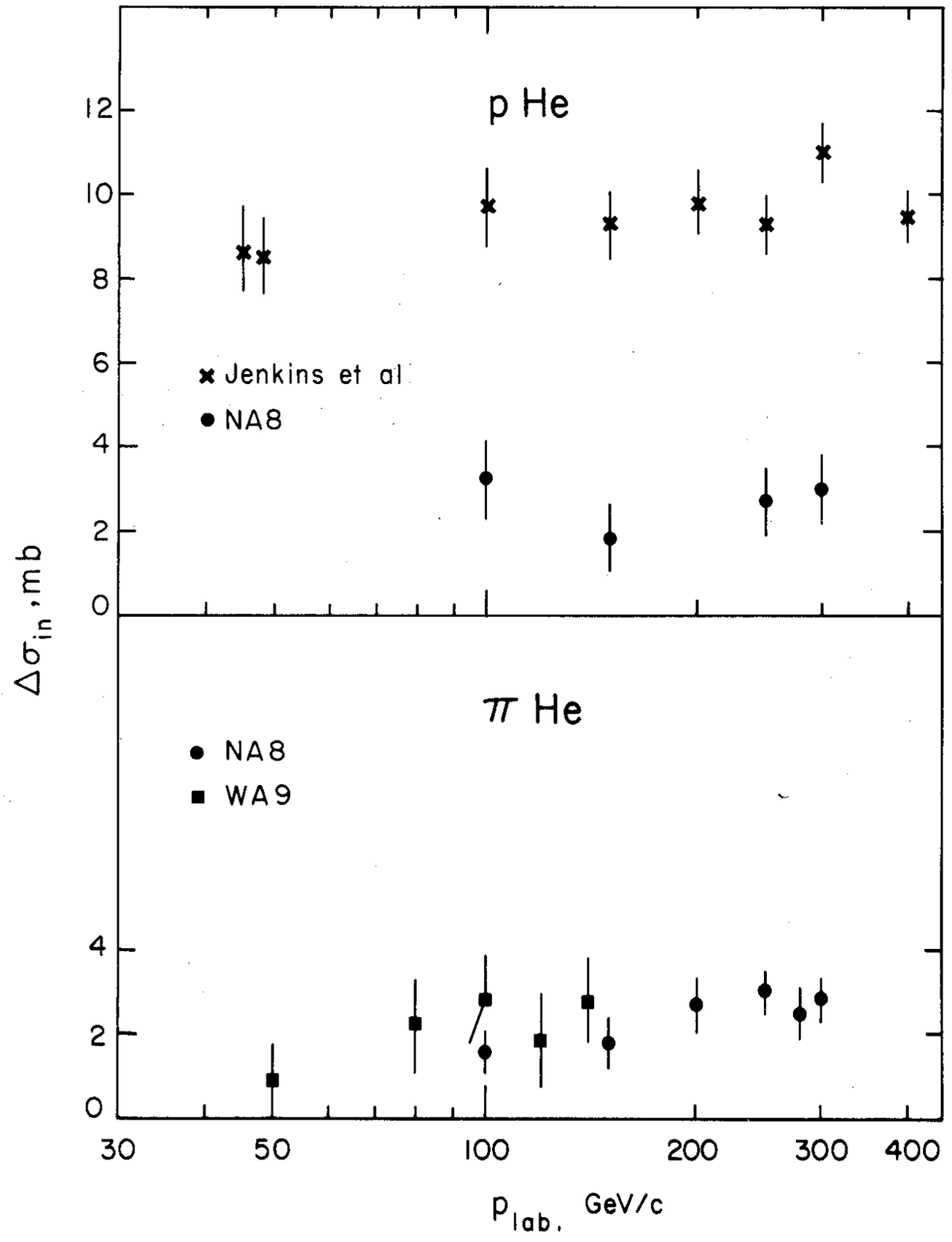
p He
Jenkins et al
NA8
π He
NA8
WA9
$\Delta\sigma_{in}$, mb
$p_{lab.}$ GeV/c
0
2
4
6
8
10
12
30
50
100
200
300
400

Fig. 9

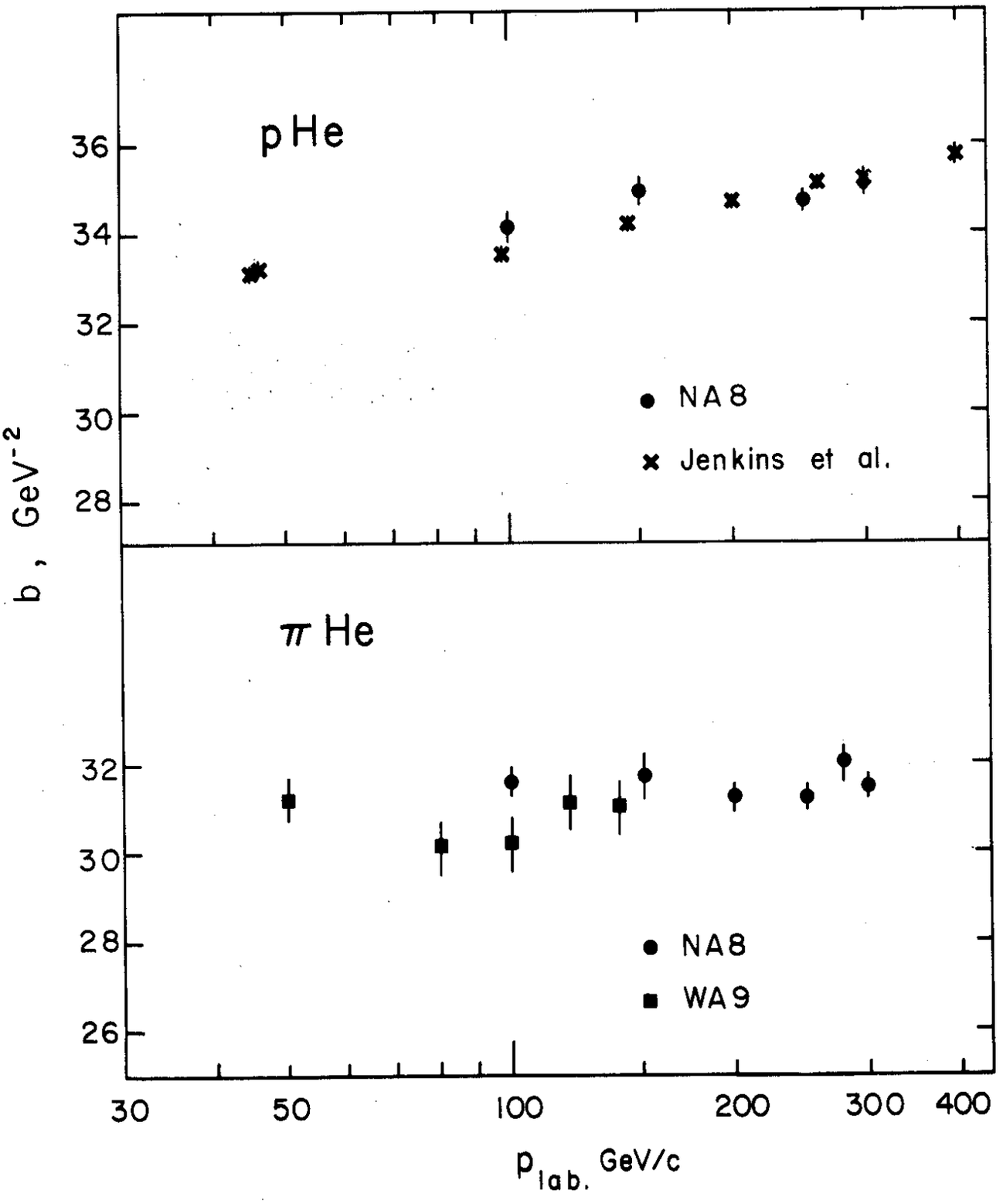
pHe
36
34
32
30
28
NA8
Jenkins et al.
b , GeV^{-2}
π He
32
30
28
26
NA8
WA9
30
50
100
200
300
400
$p_{lab.}$ GeV/c

Fig. 10

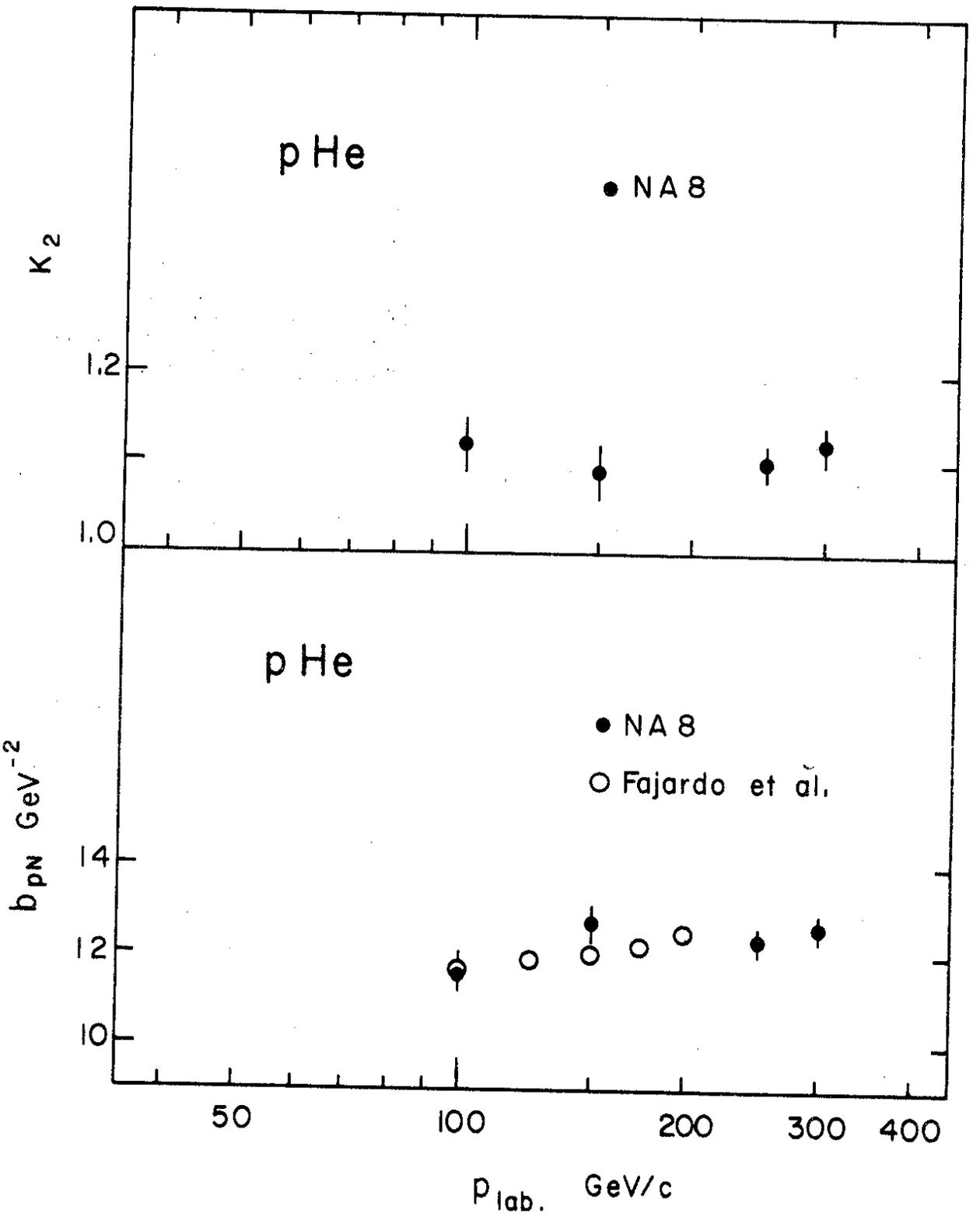
p He
● NA 8
K_2
1.2
1.0
p He
● NA 8
○ Fajardo et al.
b_{pN} GeV^{-2}
14
12
10
50
100
200
300
400
$p_{lab.}$ GeV/c

Fig. 11

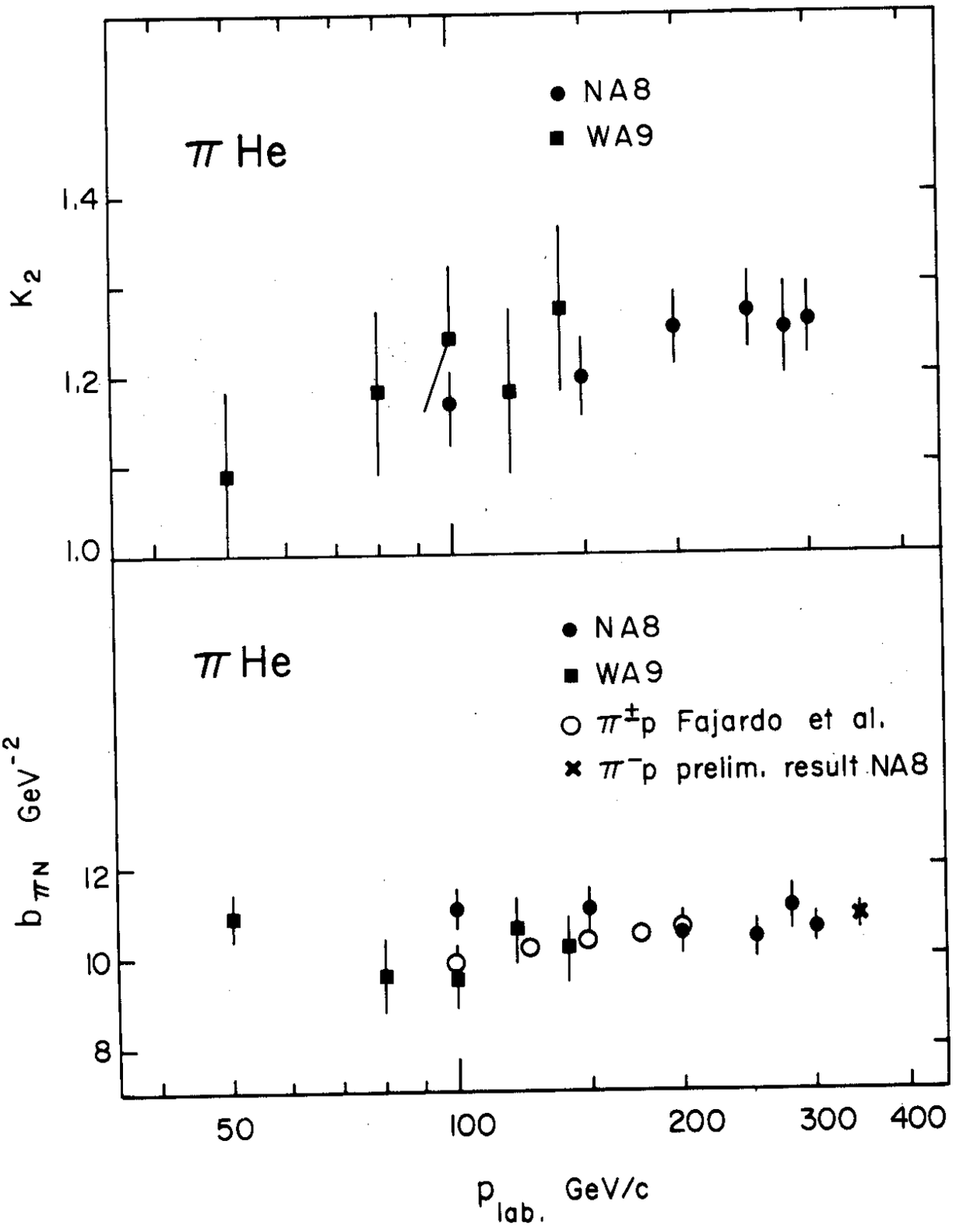
● NA8
■ WA9
π He
1.4
1.2
1.0
K2
● NA8
■ WA9
○ π±p Fajardo et al.
× π⁻p prelim. result NA8
π He
b πN GeV⁻²
12
10
8
50
100
200
300
400
p lab. GeV/c

Fig. 12